Computational Materials Science 112 (2016) 503–517

Contents lists available at ScienceDirect

Computational Materials Science

journal homepage: www.elsevier.com/locate/commatsci

Large-scale *ab initio* simulations based on systematically improvable atomic basis

Pengfei Li [a,b], Xiaohui Liu [a,b], Mohan Chen [c,*], Peize Lin [a,b], Xinguo Ren [a,b,*], Lin Lin [d], Chao Yang [e], Lixin He [a,b,*]

[a] Key Laboratory of Quantum Information, University of Science and Technology of China, Hefei 230026, China
[b] Synergetic Innovation Center of Quantum Information and Quantum Physics, University of Science and Technology of China, Hefei 230026, China
[c] Department of Mechanical and Aerospace Engineering, Princeton University, Princeton, NJ 08544, USA
[d] Department of Mathematics, University of California, Berkeley and Computational Research Division, Lawrence Berkeley National Laboratory, Berkeley, CA 94720, USA
[e] Computational Research Division, Lawrence Berkeley National Laboratory, Berkeley, CA 94720, USA

ARTICLE INFO

Article history:
Received 9 March 2015
Received in revised form 29 June 2015
Accepted 3 July 2015
Available online 13 July 2015

Keywords:
First-principles
Computer code package
Large scale
Atomic basis

ABSTRACT

We present a first-principles computer code package (ABACUS) that is based on density functional theory and numerical atomic basis sets. Theoretical foundations and numerical techniques used in the code are described, with focus on the accuracy and transferability of the hierarchical atomic basis sets as generated using a scheme proposed by Chen et al. (2010). Benchmark results are presented for a variety of systems include molecules, solids, surfaces, and defects. All results show that the ABACUS package with its associated atomic basis sets is an efficient and reliable tool for simulating both small and large-scale materials.

1. Introduction

The density functional theory [1,2] (DFT) based first-principles methods are becoming increasingly important in the research fields of condensed matter physics, material sciences, chemistry, and biology. With the rapid development of supercomputers and the advances of numerical algorithms, nowadays it is possible to study the electronic, structural and dynamical properties of complicated physical systems containing thousands of atoms using DFT. In these cases, the efficiency of widely used plane wave (PW) basis is largely limited, because of its extended nature. Instead, local bases, such as atomic orbitals, are the better choices.

Atomic orbitals have several advantages as basis sets for the *ab initio* electronic structure calculations in the Kohn–Sham scheme [1,2]. First, the basis size of atomic orbitals is much smaller compared to other basis sets, such as PW or real-space mesh. Second, the atomic orbitals are strictly localized and therefore can be combined with either the so-called linear scaling algorithms [3] for electronic calculations, or any other algorithm with a better scaling behavior than $\mathcal{O}(N^3)$. For example, Lin et al. have recently developed a so-called Pole EXpansion and Selected Inversion (PEXSI) technique [4,5], which takes advantage of the sparsity of the Hamiltonian and the overlap matrices obtained with local orbitals, and allows to solve the Kohn–Sham equations with numerical effort that scales as N^{α} ($\alpha \leq 2$) for both insulating and metallic systems, with N being the number of atoms.

While the analytical Gaussian-type orbitals have been well established for *ab initio* calculations in the quantum chemistry community for decades, the numerically tabulated atomic orbitals are getting more and more popular in the computational physics community. Several first-principles codes based on the numerical atomic orbitals have been developed in recent years, *e.g.*, SIESTA [6], OpenMX [7], FHI-aims [8], to name just a few, which aim at large-scale DFT calculations by exploiting the compactness and locality of numerical atomic orbitals. However, the numerical atomic orbitals must be constructed very carefully to ensure both good accuracy and transferability. Furthermore, it would be highly desirable if the quality of the basis sets can be systematically improved in an unbiased way. Recently, some of us [Chen, Guo, and He (CGH)] proposed a new scheme [9,10] to construct systematically improvable optimized atomic basis sets for DFT calculations. Based on the CGH procedure for basis set generations, we have developed a DFT package [11] from scratch, named

* Corresponding authors at: Key Laboratory of Quantum Information, University of Science and Technology of China, Hefei 230026, China (X. Ren, L. He).
E-mail addresses: mohan.chen.chen.mohan@gmail.com (M. Chen), renxg@ustc.edu.cn (X. Ren), helx@ustc.edu.cn (L. He).

http://dx.doi.org/10.1016/j.commatsci.2015.07.004
0927-0256/

Atomic-orbital Based Ab-initio Computation at UStc (ABACUS) here in the Key Laboratory of Quantum Information, University of Science and Technology of China (USTC). In the ABACUS package, besides the primary option of using numerical atomic orbitals as basis functions, PW basis can also be employed as an alternative choice. This dual basis feature is very useful for accuracy and consistency checks in benchmark calculations. For both basis set choices, the package uses norm-conserving pseudopotential in the Unified Pseudopotential Format (UPF) that has been used in Quantum ESPRESSO [12]. The UPF pseudopotentials can be generated from the Opium package [13]. Regarding the exchange–correlation functionals, we have implemented the local (spin) density approximation [L(S) DA], and the generalized gradient approximation (GGA) as constructed by Perdew, Burke, and Ernzerhof (PBE). In addition, semi-empirical van der Waals (vdW) corrected DFT scheme as proposed by Grimme (DFT-D2) [14] has also been implemented. Other advanced functionals such as hybrid functionals are currently under development and will be reported in a later work. At the level of local-density approximation (LDA) and generalized gradient approximation (GGA), the ABACUS package can do typical electronic structure calculations, structure relaxations, and molecular dynamics.

In this paper, we first describe the main features of the ABACUS package, as well as the major techniques that are used to implement DFT algorithms with atomic basis sets. In a previous study [9], the CGH orbitals have been demonstrated to be accurate and transferable for the group IV and group III–V semiconductors. Here, we extend the tested systems to a larger range of elements, including the alkali elements, 3d transition metals, group VI and group VII elements, with focus on the structural and electronic properties of molecules, solids, surfaces, and defects. The results demonstrate that ABACUS with the CGH orbitals are highly reliable for both finite and extended systems. In particular, the basis set at the level of double-ζ plus polarization function (DZP) is an excellent choice to compromise between accuracy and computational cost, and can be safely used in production calculations in most situations.

The rest of paper is organized as follows. In Section 2, we introduce the basic algorithms and numerical techniques. In Section 3, we will demonstrate the performance of the ABACUS package, focusing on the accuracy of the atomic orbitals generated using the CGH scheme, for a variety of benchmark systems. The scaling behavior of ABACUS for DFT–LDA calculations as a function of the system size is also presented in this section. Finally, we summarize our work in Section 4.

2. Methods

In this section, we first briefly recapitulate the basic formulation of solving Kohn–Sham equations in atomic basis (Section 2.1) to set up the stage. This is followed by a description of the main techniques used in ABACUS. Topics to be covered include the generation of the CGH atomic orbitals (Section 2.2), the construction of Hamiltonian matrix and overlap matrix (Section 2.3), the solvers for Kohn–Sham equations (Section 2.4), and finally the total energy and force calculations (Section 2.5).

2.1. The Kohn–Sham equation in atomic basis

The central task in DFT calculations is to solve the Kohn–Sham equation [1,2],

$$\widehat{H}_{\mathrm{KS}}\Psi_n(\mathbf{r}) = \epsilon_n\Psi_n(\mathbf{r}), \tag{1}$$

where ϵ_n and $\Psi_n(\mathbf{r})$ are the Kohn–Sham eigenvalues and eigenfunctions for state n. Hartree atomic unit ($e = \hbar = m_e = 1$) is used here and throughout the paper. The Kohn–Sham Hamiltonian $\widehat{H}_{\mathrm{KS}}$ can be written as,

$$\widehat{H}_{\mathrm{KS}} = \widehat{T} + \widehat{V}^{\mathrm{ext}}(\mathbf{r}) + \widehat{V}^{H}[\rho(\mathbf{r})] + \widehat{V}^{xc}[\rho(\mathbf{r})], \tag{2}$$

where $\widehat{T} = -\frac{1}{2}\nabla^2$, $\widehat{V}^{\mathrm{ext}}(\mathbf{r})$, $\widehat{V}^{H}[\rho(\mathbf{r})]$, and $\widehat{V}^{xc}[\rho(\mathbf{r})]$ are the kinetic energy operator, the external potential, the Hartree potential, and the exchange–correlation potential, respectively. The Kohn–Sham Hamiltonian $\widehat{H}_{\mathrm{KS}}$ thus depends on the electron density $\rho(\mathbf{r})$, which can be determined from the occupied Kohn–Sham orbitals

$$\rho(\mathbf{r}) = 2\sum_{n=1}^{\mathrm{occ.}}|\Psi_n(\mathbf{r})|^2. \tag{3}$$

Here for simplicity we assume that the system is spin-degenerate, and hence the spin index is omitted. Extending the algorithm described here to the spin-polarized case is straightforward and has been implemented in ABACUS.

Norm-conserving pseudopotentials are used to describe the ion–electron interactions. The external potential $\widehat{V}^{\mathrm{ext}}(\mathbf{r})$ in Eq. (2) contains the summation of the ion–electron potentials of all atoms plus, when they exist, applied external potentials. Therefore (in the absence of the applied external potential),

$$\widehat{V}^{\mathrm{ext}}(\mathbf{r}) = \sum_{\mathbf{R}}\sum_{\alpha i}\hat{v}^{ps}_{\alpha}(\mathbf{r} - \boldsymbol{\tau}_{\alpha i} - \mathbf{R}), \tag{4}$$

where $\hat{v}^{ps}_{\alpha i}$ is a norm-conserving pseudopotential [15] for the i-th atom of element type α, and $\boldsymbol{\tau}_{\alpha i}$ is the atomic coordinate in the cell $\mathbf{R}$. The pseudopotential can split into a local part of the potential $\hat{v}^{L}_{\alpha}$ and separable fully non-local potentials [16] $\hat{v}^{NL}_{\alpha}$,

$$\hat{v}^{ps}_{\alpha} = \hat{v}^{L}_{\alpha} + \hat{v}^{NL}_{\alpha}. \tag{5}$$

The applied external potentials, *e.g.*, electric fields, can be easily added to the local part of the potential, while the non-local pseudopotential can be written as,

$$\hat{v}^{NL}_{\alpha} = \sum_{l=0}^{l_{max}}\sum_{m=-l}^{l}\sum_{n=1}^{n_{max}}|\chi_{\alpha lmn}\rangle\langle\chi_{\alpha lmn}|, \tag{6}$$

where $|\chi_{\alpha lmn}\rangle$ are non-local projectors, with l, m, n being the angular momentum, the magnetic momentum, and the multiplicity of projectors, respectively. In Eq. (6), l_{max} and n_{max} are the maximal angular momentum and the maximal multiplicity of projectors for each angular momentum channel, respectively.

The Kohn–Sham equation is usually solved within certain basis sets. The ABACUS package offers two choices of basis sets: the PW basis set and the atomic basis set. The advantage to do so is that the results obtained using atomic basis sets can be directly compared to those obtained from PW basis sets for small systems, and thus provides valuable benchmarks for the former. This will be clearly seen in Section 3 where the benchmark results for a variety of systems are presented. However, since the PW algorithm has been well developed and documented, here we only focus on the algorithms of the atomic-basis implementation.

Without losing generality, we consider crystalline systems under periodic boundary conditions. The Kohn–Sham eigenfunctions in Eq. (1) then become Bloch orbitals which, within atom-centered basis set, can be expanded as,

$$\Psi_{n\mathbf{k}}(\mathbf{r}) = \frac{1}{\sqrt{N}}\sum_{\mathbf{R}}\sum_{\mu}c_{n\mu,\mathbf{k}}e^{i\mathbf{k}\cdot\mathbf{R}}\phi_{\mu}(\mathbf{r} - \boldsymbol{\tau}_{\alpha i} - \mathbf{R}), \tag{7}$$

where $\phi_{\mu}(\mathbf{r} - \boldsymbol{\tau}_{\alpha i} - \mathbf{R})$ are the atomic orbitals centering on the i-th atom of type α in the unit cell $\mathbf{R}$. The orbital index μ is a compact one, $\mu = \{\alpha, i, l, m, \zeta\}$ with l being the angular momentum, m the magnetic quantum number, and ζ the number of atomic orbitals for a given l. Here n and $\mathbf{k}$ are the band index and Bloch wave vector,

and $c_{n\mu,\mathbf{k}}$ are the Kohn–Sham eigen-coefficients. Finally N is the number of unit cells in the Born-von-Karmen supercell under the periodic boundary conditions. Using Eq. (7), the electron density within atom-centered basis sets can be computed as

$$\begin{aligned}\rho(\mathbf{r}) &= \frac{1}{N_k}\sum_{n\mathbf{k}} f_{n\mathbf{k}}\Psi^*_{n\mathbf{k}}(\mathbf{r})\Psi_{n\mathbf{k}}(\mathbf{r}) \\ &= \frac{1}{N_k}\sum_{\mathbf{R}}\sum_{\mu\nu}\sum_{n\mathbf{k}} f_{n\mathbf{k}}c^*_{\mu n,\mathbf{k}}c_{\nu n,\mathbf{k}}e^{-i\mathbf{k}\cdot\mathbf{R}}\phi^*_\mu(\mathbf{r}-\tau_{\alpha i}-\mathbf{R})\phi_\nu(\mathbf{r}-\tau_{\beta j}) \\ &= \sum_{\mathbf{R}}\sum_{\mu\nu}\rho_{\mu\nu}(\mathbf{R})\phi_\mu(\mathbf{r}-\tau_{\alpha i}-\mathbf{R})\phi_\nu(\mathbf{r}-\tau_{\beta j}),\end{aligned} \tag{8}$$

where $f_{n\mathbf{k}}$ is the Fermi occupation factor, and N_k is the number of $\mathbf{k}$ points in the Brillouin zone (BZ) sampling, which is typically equivalent to the number of real-space unit cells N in the Bloch summation. $\rho_{\mu\nu}(\mathbf{R})$ in Eq. (8) is the density matrix in real space, defined as

$$\rho_{\mu\nu}(\mathbf{R}) = \frac{1}{N_k}\sum_{n\mathbf{k}} f_{n\mathbf{k}}c^*_{n\mu,\mathbf{k}}c_{n\nu,\mathbf{k}}e^{-i\mathbf{k}\cdot\mathbf{R}}. \tag{9}$$

Please note that in the last line of Eq. (8), we have assumed, without losing generality, the atomic orbitals to be real, *i.e.*, $\phi^*_\mu = \phi_\mu$.

Given the expansion of the Kohn–Sham states in terms of atomic orbitals in Eq. (7), the Kohn–Sham equation Eq. (1) becomes a generalized eigenvalue problem,

$$H(\mathbf{k})c_{\mathbf{k}} = E_{\mathbf{k}}S(\mathbf{k})c_{\mathbf{k}}, \tag{10}$$

where $H(\mathbf{k}), S(\mathbf{k})$ and $c_{\mathbf{k}}$ are the Hamiltonian matrix, overlap matrix and eigenvectors at a given $\mathbf{k}$ point, respectively. $E_{\mathbf{k}}$ is a diagonal matrix whose entries are the Kohn–Sham eigenenergies. To obtain the Hamiltonian matrix $H(\mathbf{k})$, we first calculate

$$H_{\mu\nu}(\mathbf{R}) = \langle\phi_{\mu\mathbf{R}}|\widehat{T} + \widehat{V}^{\text{ext}} + \widehat{V}^{H} + \widehat{V}^{xc}|\phi_{\nu 0}\rangle, \tag{11}$$

where μ, ν are atomic orbital indices within one unit cell, and $\phi_{\mu\mathbf{R}} = \phi_\mu(\mathbf{r}-\mathbf{R}-\tau_{\alpha i})$, $\phi_{\nu 0} = \phi_\nu(\mathbf{r}-\tau_{\beta j})$. The Hamiltonian matrix at a given $\mathbf{k}$ point can be obtained as,

$$H_{\mu\nu}(\mathbf{k}) = \sum_{\mathbf{R}} e^{-i\mathbf{k}\cdot\mathbf{R}}H_{\mu\nu}(\mathbf{R}). \tag{12}$$

Similarly, the overlap matrix at a given $\mathbf{k}$ point is obtained as,

$$S_{\mu\nu}(\mathbf{k}) = \sum_{\mathbf{R}} e^{-i\mathbf{k}\cdot\mathbf{R}}S_{\mu\nu}(\mathbf{R}), \tag{13}$$

where

$$S_{\mu\nu}(\mathbf{R}) = \langle\phi_{\mu\mathbf{R}}|\phi_{\nu 0}\rangle. \tag{14}$$

The construction of $H(\mathbf{k})$ and $S(\mathbf{k})$, as well as solving Eq. (10) take most of the computational time. These two aspects will be discussed in more details in Sections 2.3 and 2.4.

In many cases, when the investigated unit cell is large enough, a single Γ-point in the BZ is enough to get converged results. In these cases, both the Hamiltonian and overlap matrices are real symmetric matrices. In the ABACUS package, we treat the Γ-point only calculations separately to improve the efficiency.

2.2. Systematically improvable atomic basis sets

Before going into the construction processes of $H_{\mu\nu}(\mathbf{R})$ and $S_{\mu\nu}(\mathbf{R})$, here we introduce the CGH atomic orbitals that are used in ABACUS. The quality of atomic basis is essential to obtain accurate results. Unlike PW basis, with which the quality of the calculations can be systematically improved by simply increasing the PW energy cutoff, the way to generate high-quality atomic basis functions is much more complicated. In the last decades, considerable efforts have been devoted to developing high quality atomic orbitals [7,17–20]. ABACUS adopts a scheme proposed by CGH [9] to generate systematically improvable, optimized atomic basis sets.

An atomic basis function can be written as a radial function multiplied by spherical harmonics (in practice we use solid spherical harmonic functions, which are real functions),

$$\phi_{lm\zeta}(\mathbf{r}) = f_{l\zeta}(r)Y_{lm}(\hat{r}), \tag{15}$$

where the indices l, m, and ζ have the usual meanings of angular momentum quantum number, magnetic quantum number, and the multiplicity of the orbitals for l. One usually needs more than one radial functions for each angular momentum to improve the quality and transferability of the atomic basis sets.

In the CGH scheme, the radial function $f_{l\zeta}(r)$ is expanded in terms of a set of spherical Bessel functions (SBFs), with the coefficients of the SBFs yet to be determined, *i.e.*,

$$f_{l\zeta}(\mathbf{r}) = \begin{cases}\sum_q c_{l\zeta q}j_l(qr), & r < r_c \\ 0 & r \geqslant r_c,\end{cases} \tag{16}$$

where $j_l(qr_c)$ is the SBF with radius cutoff r_c. The possible q values are chosen such that $j_l(qr_c) = 0$. A kinetic energy cutoff is chosen to determine the maximal value of q, and thus the number of SBFs. We set the SBFs to be strictly zero beyond the radius cutoff r_c. In fact, they have been used directly as short-ranged basis set in first-principles calculations [21,22]. Because (almost) any function within the radius cutoff r_c can be represented as a linear combination of SBFs, this gives us a large number of degrees of freedom for optimizing the atomic basis set.

To obtain optimized atomic basis, we vary the coefficients of the SBFs to minimize the spillage between the atomic basis set and a set of selected reference systems. The spillage $\mathcal{S}$ is a positive number defined as the difference between the Hilbert space spanned the atomic basis set and the wave functions calculated by PW basis,

$$\mathcal{S} = \frac{1}{N_n N_{\mathbf{k}}}\sum_{n=1}^{N_n}\sum_{\mathbf{k}=1}^{N_{\mathbf{k}}}\langle\Psi_{n\mathbf{k}}|1-\widehat{P}_{\mathbf{k}}|\Psi_{n\mathbf{k}}\rangle, \tag{17}$$

where $\widehat{P}$ is a projector spanned by the atomic orbitals,

$$\widehat{P}_{\mathbf{k}} = \sum_{\mu\nu}|\phi_{\mu,\mathbf{k}}\rangle S^{-1}_{\mu\nu}(\mathbf{k})\langle\phi_{\nu,\mathbf{k}}|. \tag{18}$$

Here, $S^{-1}(\mathbf{k})$ is the inverse of overlap matrix $S(\mathbf{k})$ between numerical atomic orbitals. The spillage has been proposed before to measure the quality of a set of atomic basis [18,23,24]. We then use simulated annealing method to determine the coefficients that minimize the spillage. Sometimes the numerical orbitals obtained from this procedure have unphysical oscillations, which may lower the transferability of the basis set. To eliminate these unphysical oscillations, we further minimize the kinetic energy of each atomic orbital while keeping the spillage almost unchanged. More details of this procedure can be found in Ref. [9].

The reference systems used in the basis-generation procedure are very important to ensure the transferability of numerical atomic orbitals. The CGH scheme allows the users to choose freely the target systems to generate high-quality basis sets for different purposes. From our experience, homonuclear dimers are very good reference systems [17,25] for generating transferable atomic orbitals for general purposes. To avoid any possible bias of the basis set towards certain geometrical structure, an average over dimers of several different bond lengths (compressed or elongated) is taken as the target in the optimization procedure. We provide scripts to generate the atomic bases using diatomic molecules as reference systems. The scripts set up PW calculations provided in the code

for the dimers at various bond lengths. We remark that after the atomic basis sets are generated, for consistency, one must use the same pseudopotential and energy cutoff in later atomic orbitals based calculations as those used in the basis generation.

The CGH scheme is very flexible and easy to implement. One can choose freely the angular momentum of the orbitals, and the multiplicity of the radial functions for each angular momentum. All atomic orbitals are generated from the same procedure and criteria. These orbitals form a sequence of hierarchial basis sets, which have a systematic convergence behavior towards the PW reference. Furthermore, without any assumptions of the shapes of radial functions $f_{l\zeta}(r)$, in principle we can get the fully optimized radial functions. As will be shown in Section 3, the atomic orbitals generated in this way indeed show excellent accuracy and transferability for various systems.

2.3. Hamiltonian and overlap matrices construction

As mentioned above, in order to construct $H(\mathbf{k})$ and $S(\mathbf{k})$ at given $\mathbf{k}$ points using Eqs. (12) and (13), we need to first calculate $H_{\mu\nu}(\mathbf{R})$ and $S_{\mu\nu}(\mathbf{R})$. During the processes, we take the full advantage of the short-range nature of the atomic orbitals, *i.e.*, only the matrix elements whose corresponding atomic orbitals have non-zero overlaps are evaluated. This is because each matrix element could be written as an integral in real-space grids, if this integral involves two spatially well-separated basis functions that are not overlapping, then the result of the integral should be zero. This feature leads to a sparse matrix and then $\mathcal{O}(N)$ scaling of the number of integrals, which is a significant advantage compared to PW based methods.

Now we briefly discuss how each term in $H_{\mu\nu}(\mathbf{R})$ and $S_{\mu\nu}(\mathbf{R})$ is calculated. As is clear from Eq. (11), the Hamiltonian matrix has several components, which are computed by two different techniques, namely the two-center integral technique and the grid integral technique, respectively. First, the kinetic energy matrix $T_{\mu\nu}(\mathbf{R}) = \langle\phi_{\mu\mathbf{R}}|\widehat{T}|\phi_{\nu 0}\rangle$, the non-local pseudopotential matrix $V^{NL}_{\mu\nu}(\mathbf{R}) = \langle\phi_{\mu\mathbf{R}}|\widehat{V}^{NL}|\phi_{\nu 0}\rangle$, as well as the overlap matrix $S_{\mu\nu}(\mathbf{R}) = \langle\phi_{\mu\mathbf{R}}|\phi_{\nu 0}\rangle$ can be efficiently calculated by the two-center integral technique [26], which has been described thoroughly in Ref. [6]. The two-center integrals can be split into two parts: a one-dimensional integral over radial functions and an angular integral involving spherical harmonic functions. The radial integrals are tabulated for a wide range of distances between two orbitals once for all. The value for two orbitals within a reasonable distance can then be interpolated from the table. The angular integral involving spherical harmonic functions leads to quantities of so-called the Gaunt coefficients, which can also be easily calculated. Therefore, the two center integrals can be evaluated very efficiently [6]. Further details on the two-center integral technique are given in Appendix A.1.

The matrix elements of the local potentials, $V^{loc}_{\mu\nu}(\mathbf{R}) = \langle\phi_{\mu\mathbf{R}}|\widehat{V}^{loc}|\phi_{\nu 0}\rangle$, with

$$V^{loc}(\mathbf{r}) = V^{L}(\mathbf{r}) + V^{H}(\mathbf{r}) + V^{xc}(\mathbf{r}) \tag{19}$$

are evaluated on a uniform grid in real space. Here $V^{L}(\mathbf{r})$ is the sum of all local pseudopotentials. We first evaluate the local potential $V^{loc}(\mathbf{r})$ on each grid point: the local pseudopotentials and Hartree potentials are calculated using techniques adapted from PW basis, *i.e.*, they are first calculated in the reciprocal space, and then Fourier transformed to the real-space grid. The exchange–correlation potential can be directly evaluated on the real-space grid. Once we have $V^{loc}(\mathbf{r})$, the matrix elements $V^{loc}_{\mu\nu}(\mathbf{R})$ are directly summed over the real-space grid. More details on the grid-based integral technique for the local potentials are given in Appendix A.2. The grid integrals are one of the most time consuming parts in the algorithms based on atomic orbitals. However, the computation efforts of the grid integrals only scale linearly with the system size, and can be easily parallelized.

2.4. Kohn–Sham equation solvers

After the Hamiltonian and overlap matrices are constructed, the Kohn–Sham equations are solved separately at each $\mathbf{k}$-point, which amounts to solving a generalized eigenvalue problem. This constitutes the major computational bottleneck for systems larger than a few hundreds of atoms. Standard diagonalization method scales as $\mathcal{O}(N^3)$, where N is the matrix dimension. There are a few parallel matrix eigenvalue solvers available. ABACUS uses a package named High Performance Symmetric Eigenproblem Solvers (HPSEPS) developed by the Supercomputing Center of Chinese Academy of Science, to diagonalize the Kohn–Sham Hamiltonian [27]. HPSEPS provides parallel solvers for generalized eigenvalue problems concerning large dimensions of matrix.

Recently, Lin et al. [28–30] developed the PEXSI technique, which provides an alternative way for solving the Kohn–Sham problem without using a diagonalization procedure. Compared to linear scaling approach, PEXSI does not rely on the nearsightedness principle either to truncate density matrix elements. In a Γ-point calculation, the basic idea of PEXSI can be illustrated as follows. Denote by M the number of atomic orbitals, $\Phi(\mathbf{r}) = [\phi_1(\mathbf{r}), \ldots, \phi_M(\mathbf{r})]$ the collection of all atomic orbitals in the real space, and $\hat{\gamma}(\mathbf{r}, \mathbf{r}')$ the single particle density matrix in the real space. Then the PEXSI approach first expands $\hat{\gamma}(\mathbf{r}, \mathbf{r}')$ using a P-term pole expansion as

$$\hat{\gamma}(\mathbf{r}, \mathbf{r}') \equiv \Phi(\mathbf{r})\Gamma\Phi^*(\mathbf{r}') \approx \Phi(\mathbf{r})\mathrm{Im}\left(\sum_{l=1}^{P}\frac{\omega_l^{\rho}}{H-(z_l+\epsilon_F)S}\right)\Phi^*(\mathbf{r}'). \tag{20}$$

Here H, S, Γ are the Hamiltonian matrix, the overlap matrix and the single particle density matrix represented under the atomic orbital basis set Φ, respectively. ϵ_F is the chemical potential or Fermi energy. The complex shifts $\{z_l\}$ and weights $\{\omega_l^{\rho}\}$ are determined through a simple semi-analytic formula, and takes negligible amount of time to compute. The number of terms of the pole expansion is proportional to $\log(\beta\Delta E)$, where β is the inverse of temperature and ΔE is the spectral radius, which can be approximated by the largest eigenvalue of the (H, S) matrix pencil. The logarithmic scaling makes the pole expansion a highly efficient approach to expand the Fermi operator.

At first it may seem that the entire Green's function-like object $[H-(z_l+\epsilon_F)S]^{-1}$ needs to be computed. However, if we target the electron density $\rho(\mathbf{r}) = \hat{\gamma}(\mathbf{r}, \mathbf{r})$, then only $\left\{\left[(H-(z_l+\epsilon_F)S)^{-1}\right]_{\mu\nu} \mid H_{\mu\nu} \neq 0\right\}$ are actually needed. A selected inversion algorithm can be used to efficiently compute these *selected elements* of the Green's function, and therefore the entire electron density. The computational cost of the PEXSI technique scales at most as $\mathcal{O}(N^2)$. The actual computational cost depends on the dimensionality of the system: the cost for quasi-1D systems such as nanotubes is $\mathcal{O}(N)$ *i.e.* linear scaling; for quasi-two-dimensional systems such as graphene and surfaces (slabs) the cost is $\mathcal{O}(N^{1.5})$; for general three-dimensional bulk systems the cost is $\mathcal{O}(N^2)$. This favorable scaling hinges on the sparse character of the Hamiltonian and overlap matrices, but not on any fundamental assumption about the localization properties of the single particle density matrix. This method is not only applicable to the efficient computation of electron density, but also to other physical quantities such as free energy, atomic forces, density of states and local density of states.

All these quantities can be obtained without computing any eigenvalues or eigenvectors. For instance, the atomic force for atom i in species α can be computed as

$$F_{\alpha i} \approx -\mathrm{Tr}\left[\Gamma \frac{\partial H}{\partial \tau_{\alpha i}}\right] + \mathrm{Tr}\left[\Gamma^E \frac{\partial S}{\partial \tau_{\alpha i}}\right], \tag{21}$$

where the first part is independent of PEXSI algorithm and will be discussed in the next subsection. The second term in Eq. (21) depends on the energy density matrix, which is written as

$$\Gamma^E \approx \mathrm{Im}\sum_{l=1}^{P} \frac{\omega_l^E}{H - (z_l + \epsilon_F)S}. \tag{22}$$

This matrix is given again by pole expansions with *the same poles* as those used for computing the charge density, with different weights $\{\omega_l^E\}$. For more detailed information we refer readers to Refs. [30,31]. In order to use the PEXSI technique for multiple **k**-point calculations, we need to work with the Green's function of a non-Hermitian Hamiltonian that is only structurally symmetric. The massively parallel selected inversion method for non-Hermitian but structurally symmetric matrices are currently under development, and will be integrated into ABACUS in the future to perform large scale electronic structure calculations with multiple **k**-point sampling.

Compared to existing techniques, the PEXSI method has some notable features: (1) The efficiency of the PEXSI technique does not depend on the existence of a finite Highest Occupied Molecular Orbital (HOMO)-Lowest Unoccupied Molecular Orbital (LUMO) gap, and can be accurately applied to general materials systems including small gapped systems and metallic systems. The method remains accurate at low temperatures. (2) The PEXSI method has a two-level parallelism structure and is by design highly scalable. The recently developed massively parallel PEXSI technique can make efficient use of 10,000–100,000 processors on high performance machines. (3) As a Fermi operator expansion based method, PEXSI allows the use of a hybrid scheme that combines density of states estimation based on Sylvester's law of inertia with Newton's method to obtain the chemical potential. This is a highly efficient and robust approach with respect to the initial guess of the chemical potential, and is independent of the presence of gap states. (4) PEXSI can be controlled with a few input parameters, and can act nearly as a black-box substitution of the diagonalization procedure commonly used in electronic structure calculations.

In order to benefit from the PEXSI method, the Hamiltonian and overlap matrices must be sparse, and this requirement is satisfied when atomic orbitals are used to discretize the Kohn–Sham Hamiltonian. The sequential version of PEXSI has been demonstrated before with ABACUS [30], and the massively parallel version of PEXSI is recently integrated with SIESTA [31] for studying large scale systems with more than 10,000 atoms with insulating and metallic characters on more than 10,000 processors. The parallel PEXSI method is to be integrated with ABACUS.

2.5. Total energy and force calculations

Once the Kohn–Sham equation is solved, one can obtain the total energy of the system using the Harris functional [32],

$$E^{tot} = E^{band} - \int V^{Hxc}(\mathbf{r})\rho(\mathbf{r})d\mathbf{r} + E^H + E^{xc} + E^{II}, \tag{23}$$

where E^{band} is the Kohn–Sham band energy, which is the summation over occupied Kohn–Sham orbital energies. E^H, E^{xc} and E^{II} are the Hartree energy, the exchange–correlation energy, and the Coulomb energy between ions respectively. The second term in the above equation is the so-called double-counting energy arising from the Hartree and exchange–correlation potential, which have been included in the band energy term. If the Kohn–Sham equation is solved by matrix diagonalization, then the band energy is the summation of the Kohn–Sham eigenvalues $\epsilon_{n\mathbf{k}}$ of all occupied bands, *i.e.*,

$$E^{band} = \frac{1}{N_k}\sum_{n\mathbf{k}} f_{n\mathbf{k}}\epsilon_{n\mathbf{k}}. \tag{24}$$

Alternatively, if the PEXSI method is chosen to be the Kohn–Sham equation solver, the band energy is calculated as (only for Γ-point now)

$$E^{band} = \mathrm{Tr}[\rho H], \tag{25}$$

where ρ is the density matrix and H is the Hamiltonian matrix. The Hartree and exchange–correlation energies are calculated on a uniform real-space grid, and E^{II} are calculated by the Ewald summation technique [33].

The forces acting on the ions are given by the derivative of the total energy with respect to the atomic coordinates. Analytical expressions for forces computed with atomic basis sets are more sophisticated than those with the PW basis sets. Besides the Feynman–Hellmann forces, Pulay forces [34] due to the change of the atomic basis sets during a structural relaxation should also be considered.

Therefore, we rewrite the total energy as the sum of two parts: $E^{tot} = E^{KS} + E^{II}$, where E^{KS} is the electronic part of the total energy in Eq. (23), while E^{II} is the energy due to the Coulomb interactions between ions. Then the total force experienced by the i-ion of type α is

$$F_{\alpha i} = -\frac{\partial E^{tot}}{\partial \tau_{\alpha i}} = -\frac{\partial E^{KS}}{\partial \tau_{\alpha i}} - \frac{\partial E^{II}}{\partial \tau_{\alpha i}}. \tag{26}$$

After some derivations (more details are given in Appendix A.3), we arrive at

$$\frac{\partial E^{KS}}{\partial \tau_{\alpha i}} = \sum_{\mathbf{R}}\sum_{\mu\nu}\rho_{\mu\nu}(\mathbf{R})\frac{\partial H_{\mu\nu}(\mathbf{R})}{\partial \tau_{\alpha i}} + \sum_{\mathbf{R}}\sum_{\mu\nu}\frac{\partial \rho_{\mu\nu}(\mathbf{R})}{\partial \tau_{\alpha i}}H_{\mu\nu}(\mathbf{R}), \tag{27}$$

with

$$\frac{\partial H_{\mu\nu}(\mathbf{R})}{\partial \tau_{\alpha i}} = \left\langle \phi_{\mu\mathbf{R}}\middle|\frac{\partial H}{\partial \tau_{\alpha i}}\middle|\phi_{\nu 0}\right\rangle + \left\langle \frac{\partial \phi_{\mu\mathbf{R}}}{\partial \tau_{\alpha i}}\middle|H\middle|\phi_{\nu 0}\right\rangle + \left\langle \phi_{\mu\mathbf{R}}\middle|H\middle|\frac{\partial \phi_{\nu 0}}{\partial \tau_{\alpha i}}\right\rangle. \tag{28}$$

Note that $\mu = \{\alpha, i, l, m, \zeta\}$ is the compact index for the atomic orbitals. The first term of the above equation is the Feynman–Hellmann force [35], whereas the rest two terms yield the so-called Pulay forces [34]. Following Ref. [6], one can prove that the term related to $\frac{\partial \rho_{\mu\nu}(\mathbf{R})}{\partial \tau_{\alpha i}}$ is

$$\sum_{\mathbf{R}}\sum_{\mu\nu}\frac{\partial \rho_{\mu\nu}(\mathbf{R})}{\partial \tau_{\alpha i}}H_{\mu\nu} = \sum_{\mathbf{R}}\sum_{\mu\nu}E_{\mu\nu}(\mathbf{R})\frac{\partial S_{\mu\nu}(\mathbf{R})}{\partial \tau_{\alpha i}}, \tag{29}$$

where

$$E_{\mu\nu}(\mathbf{R}) = \frac{1}{N_k}\sum_{n\mathbf{k}} f_{n\mathbf{k}}\epsilon_{n\mathbf{k}}c^*_{\mu n,\mathbf{k}}c_{n\nu,\mathbf{k}}e^{-i\mathbf{k}\cdot\mathbf{R}}, \tag{30}$$

is the element of "energy density matrix". In the above equation, ϵ_{nk} is the band energy for band n at wave vector **k**. This term arises because the atomic orbitals are not orthogonal.

Similar to the total energy evaluation, different force terms are also evaluated using different techniques to maximize the efficiency of force calculations. Specifically, due to the long range tail of local pseudopotential in real space, it is better to calculate it in reciprocal space using PW basis set, and this is how Feynman–

Hellmann force associated with the local pseudopotentials is implemented. Another advantage of this implementation is that the derivative of the local pseudopotential can be easily done in reciprocal space. By taking advantage of the short-range character of the non-local pseudopotential operators and atomic orbitals, the force terms including the Feynman–Hellmann force arising from the non-local pseudopotential operator, the Pulay forces arising from the kinetic energy operator, as well as the non-orthogonal forces, are calculated using two-center integral techniques. Finally, the Pulay forces associated with the local potentials are evaluated by grid integrals. Here the local pseudopotentials are first evaluated in reciprocal space and Fourier transformed to a real-space mesh. Technical details on the force calculations can be found in Appendix A.3.

With the capability of calculating forces efficiently, a structural relaxation can be done by searching the local minimum in potential energy surface. Two algorithms for structural relaxations are implemented, namely the Broyden–Fletcher–Goldfarb–Shanno (BFGS) method [36] and the conjugate gradient (CG) method [37].

3. Results

In this section, benchmark results obtained from ABACUS are presented for a variety of systems, including molecules, crystalline solids, surfaces, and defects. The tested atomic species cover both main-group elements and transition metal elements. In particular, the convergence of calculated physical properties are tested with respect to the size of CGH orbitals. The tested basis sets form a hierarchy by spanning from single-ζ (SZ), double-ζ (DZ), double-ζ plus polarization functions (DZP), to triple-ζ plus double polarization functions (TZDP), and quadrupole-ζ plus triple polarization functions (QZTP). In the following tests, we refer to these basis sets as atomic basis sets, or equivalently, as linear combination of atomic orbitals (LCAO). The references for the tested properties are chosen to be those calculated by converged PW basis set with the same pseudopotentials. Available experimental results are also included for comparisons.

The naming of basis sets depends on the valence electrons of each element. For example, SZ refers to a single s orbital for elements that have only s valence electrons, such as alkali metal elements. For elements that have p valence electrons, SZ refers to a single s orbital plus three p orbitals, such as first- and second-row non-metal elements. Furthermore, for transition metal elements, SZ refers to one s orbital, three p orbitals plus five d orbitals. Here the number of orbitals on each angular momentum channel is $(2l+1)$, where l is the angular momentum quantum number. The polarization functions refer to orbitals that have higher l than the maximal one used in a SZ basis set. Specifically, in a SZ basis set that contains only one s orbital, the p orbitals are referred to the polarization functions; in a SZ basis set that has both s and p orbitals, the d orbitals are indicated as the polarization functions. Finally, for transition metals which use all s, p, d orbitals in a SZ basis set, the f orbitals are the polarization functions.

Two more parameters are needed to define a CGH atomic orbital. First, because CGH atomic orbitals are generated by an optimization procedure that is based on the results from PW calculations of target systems (typically diatomic molecules here), thus the generated set of atomic orbitals depend on a specific energy cutoff (E_{cut}) used in PW calculations. Second, all CGH atomic orbitals are enforced to be strictly localized within a radius R_{cut}, beyond which the atomic orbitals are set to be exactly zero. Table 1 lists both parameters for 24 elements that will be used in the followings to test physical properties of systems.

Table 1
Energy cutoff E_{cut} (in Ry) and radius cutoff R_{cut} (in Bohr) parameters of the LCAO basis functions for 24 different elements used in this paper.

Element	E_{cut} (Ry)	R_{cut} (Bohr)	Element	E_{cut} (Ry)	R_{cut} (Bohr)
H	50	6	Cl	50	8
Li	30	12	Ti	100	10
C	50	8	Fe	100	10
N	50	8	Cu	100	8
O	50	8	Ga	50	9
F	50	8	Ge	50	9
Na	20	12	As	50	9
Mg	20	12	Br	50	9
Al	50	9	Br	50	9
Si	50	8	In	50	9
P	50	9	Sb	50	9
S	50	8	I	50	9

Compared to a PW basis set which can be systematically increased to reach arbitrary accuracy in a calculation, the accuracy of the existing LCAO basis sets are known to be difficult to improve systematically. However, our construction strategy for numerical atomic orbitals described in Section 2.2 can in principle guarantees a systematic convergence towards the PW accuracy for the target system. We note that, for general systems, the convergence behavior of an atomic basis set should be checked *a posteriori*. This is carried out separately for molecules in Section 3.2 and for solids in Section 3.3. Among all these tests, first of all, let us look into one numerical issue that is very common in atomic-orbital based calculations – the so-called eggbox effect [38] – which occurs when the integrals of matrix elements are evaluated on a finite, uniformly spaced real-space grid.

3.1. Eggbox effect

The eggbox effect refers to the artificial rippling of the ground-state total energy as a function of the atomic displacements relative to an uniform real-space grid points [38,39]. Specifically, it arises from the numerical errors in evaluating the integrals of a Hamiltonian operator with respect to the local orbitals on a finite uniform real-space grid. This effect is completely artificial but considerably complicates the calculations of forces acting on atoms and phonon dispersions. Naturally, the denser the real-space grid is – corresponding to a higher energy cutoff in the reciprocal space, the smaller in magnitude that the rippling of the ground-state total energy will be. Conversely, if an atomic orbital in the real space is designed in a cautious way that the high-energy components of its Fourier transform are suppressed, then a less denser real-space grid is needed. Based on this principle, Anglada and Soler proposed an efficient filtering procedure [38] to effectively suppress the high-energy components of their local orbitals, without sacrificing the locality of these basis functions. This procedure has been shown to work well in the SIESTA package [40]. In the ABACUS package, our basis functions are automatically confined in the reciprocal space below a certain energy cutoff during the construction processes.

Consequently, we show the simulated results for diatomic molecules Si_2, O_2, and Mn_2 at their equilibrium distances in Fig. 1. Unless otherwise stated, the molecular calculations are all done under the periodic boundary conditions. A cubic box with a side length of 20 Bohr is chosen for all three molecules. The atomic basis set is chosen to be DZP. As illustrated in Fig. 1, the eggbox effects are exceedingly small for these molecules. In particular, for Si_2 and O_2, the oscillations of the total energy are within 1 meV, while the force oscillations are within 1 meV/Å. The oscillation of force for Mn_2 is most pronounced, but is still within 10 meV/Å. This accuracy is sufficient for most practical purposes.

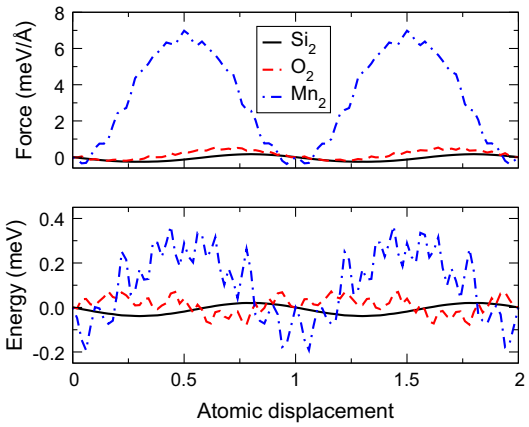

Fig. 1. Eggbox effects for Si_2, O_2, and Mn_2 molecules. The unit in the *x* axis is the spacing between neighboring real-space grid points, which amounts to 0.21 Bohr for an energy cutoff of 50 Ry.

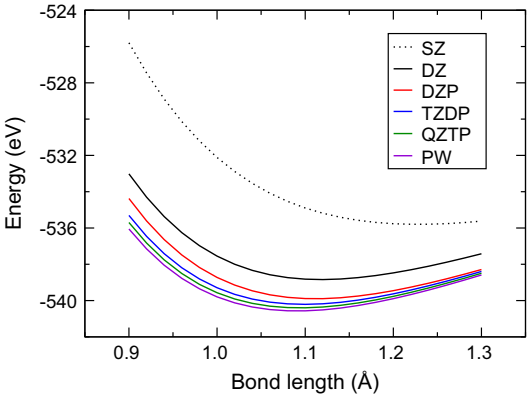

Fig. 2. Total energy of the N_2 molecule as a function of the bond length for a sequence of increasing LCAO basis sets. The PW results are also shown for comparison.

On top of these oscillation patterns, the additional wiggling patterns of the energy and force curves for O_2 and Mn_2 have not been well understood, but these only occur at a smaller energy scale and have not caused any problems so far. As will be shown in Section 3.4, accurate structural relaxations can be carried out without further corrections for the eggbox effect.

3.2. Molecules

Having the eggbox effect under control, we now look into the convergence quality of atomic basis set for small molecules. Similar to the eggbox test cases, a cubic cell with a side length 20 Bohr is chosen here to avoid the artificial interactions between a molecule and its images. Taking N_2 as an example, we plot its ground-state energy versus its bond distance in Fig. 2. The hierarchical basis sets using in this calculation range from SZ to QZTP. The reference is obtained from PW calculations. As illustrated in Fig. 2, as the size of the atomic basis set increases, the total energy of the N_2 molecule converges systematically towards the PW limit. From these curves, one can deduce the equilibrium bond length, atomization energy, and vibrational frequency of the N_2 molecule. These quantities obtained with atomic basis sets for a selected molecular set can be used to validate the convergence quality of the localized basis sets, when compared to the corresponding results obtained from PW calculations.

In the followings, we present the benchmark results for bond lengths, atomization energies, and vibrational frequencies for 11 chemically bonded diatomic molecules. Followed by the interaction energies of the S22 molecular test set [41], obtained by the DFT-D method [14] as implemented in ABACUS. The first test is used to validate our methods for chemically bonded dimers while the second one is for weakly bonded systems.

3.2.1. Bond lengths

The bond length of a molecule is an important quantity. In Table 2, the calculated bond lengths of 11 diatomic molecules are presented for atomic basis sets range from SZ to QZTP. The PW results are also shown, and the experimental data are taken from Refs. [42,43]. Both LDA [2,44] and PBE [45] exchange–correlation functionals are used.

As shown in Table 2, all the calculated equilibrium bond lengths systematically approach the corresponding PW results with increased atomic orbital basis sets. Specifically, the mean absolute error (MAE) for the DZP basis set is 0.018 Å for both LDA and PBE calculations. This accuracy is sufficiently good for most practical purposes. When going beyond DZP to TZDP and QZTP basis sets, the MAEs become even smaller; at the QZTP level, the MAE is only 0.004 Å for LDA and 0.003 Å for PBE.

For alkali-metal elements, the construction of high-quality localized atomic orbitals [6,46] is highly challenging because these orbitals tend to be very diffusive and have a longer tail than the atomic orbitals of other elements. However, by using CGH orbitals, we found that a rather satisfactory description of the molecular bonding involving alkali metal atoms can be achieved, as can be seen from the examples of Na_2 and LiH in Table 2, if a large cutoff radius, *i.e.,* between 10 Bohr and 12 Bohr, is used. The same observation holds for alkali metal elements in bulk materials, as will be shown in Section 3.3.

The experimental values in Table 2 are only shown for comparison purpose, and not for benchmark purpose. In all tests of bond

Table 2
Bond lengths (in Å) of diatomic molecules obtained with various sets of atomic orbitals, in comparison with PW results and experimental data (EXP). Both LDA and PBE results are shown. The MAEs of atomic basis sets are obtained with reference to the PW results.

Molecules	SZ	DZ	DZP	TZDP	QZTP	PW	EXP
LDA							
N_2	1.227	1.121	1.107	1.098	1.096	1.095	1.098
O_2	1.086	1.132	1.192	1.195	1.196	1.198	1.208
S_2	1.683	1.724	1.852	1.869	1.870	1.871	1.889
F_2	1.304	1.331	1.398	1.402	1.402	1.405	1.412
Cl_2	1.848	1.877	1.932	1.949	1.951	1.952	1.988
Br_2	2.035	2.184	2.211	2.226	2.233	2.240	2.281
I_2	2.479	2.563	2.608	2.623	2.634	2.641	2.665
Li_2	2.503	2.570	2.627	2.639	2.639	2.642	2.673
Na_2	2.901	2.972	3.028	3.038	3.041	3.053	3.079
CO	1.271	1.157	1.136	1.125	1.125	1.123	1.128
LiH	1.659	1.688	1.621	1.597	1.597	1.599	1.595
MAE	0.137	0.072	0.018	0.006	0.004	/	/
PBE							
N_2	1.253	1.167	1.109	1.103	1.103	1.101	1.098
O_2	1.289	1.251	1.225	1.218	1.214	1.211	1.208
S_2	1.981	1.929	1.903	1.892	1.891	1.891	1.889
F_2	1.319	1.352	1.402	1.413	1.416	1.418	1.412
Cl_2	2.195	2.087	2.019	2.006	2.003	2.001	1.988
Br_2	2.457	2.396	2.330	2.313	2.304	2.292	2.281
I_2	2.837	2.782	2.718	2.693	2.681	2.674	2.665
Li_2	2.770	2.710	2.699	2.690	2.690	2.687	2.673
Na_2	3.265	3.187	3.103	3.094	3.094	3.092	3.079
CO	1.140	1.133	1.130	1.129	1.129	1.129	1.128
LiH	1.748	1.668	1.612	1.608	1.607	1.605	1.595
MAE	0.133	0.065	0.018	0.007	0.003	/	/

Table 3
Atomization energies (in eV) of molecules obtained with various sets of atomic orbitals, in comparison with PW and experimental results (EXP). The MAEs of atomic basis sets are obtained with reference to the PW basis set.

Molecule	SZ	DZ	DZP	TZDP	QZTP	PW	EXP
LDA							
N_2	6.882	9.566	11.007	11.162	11.183	11.193	9.759
O_2	5.636	6.495	7.437	7.491	7.506	7.542	5.117
S_2	3.990	4.540	4.850	4.944	4.985	5.006	4.370
F_2	0.746	0.995	1.834	1.876	1.886	1.917	1.601
Cl_2	1.430	1.648	2.871	2.912	2.912	2.943	2.480
Br_2	1.698	2.086	2.342	2.381	2.393	2.412	1.971
I_2	1.179	1.457	1.931	1.943	1.965	1.984	1.542
Li_2	1.323	1.135	1.111	1.106	1.104	1.083	1.037
Na_2	1.134	0.998	0.964	0.933	0.933	0.902	0.735
CO	10.252	11.099	12.722	12.741	12.754	12.758	11.108
LiH	1.585	2.218	2.633	2.684	2.684	2.664	2.415
MAE	1.408	0.769	0.080	0.034	0.022	/	/
PBE							
N_2	6.389	8.727	10.375	10.592	10.592	10.623	9.759
O_2	4.712	5.183	6.043	6.133	6.145	6.190	5.117
S_2	4.032	4.467	4.602	4.664	4.747	4.788	4.370
F_2	0.852	1.239	1.786	1.815	1.820	1.834	1.601
Cl_2	1.552	2.196	2.682	2.714	2.721	2.734	2.480
Br_2	1.329	1.783	2.024	2.065	2.086	2.105	1.971
I_2	1.085	1.293	1.642	1.685	1.704	1.728	1.542
Li_2	1.306	1.124	1.096	1.088	1.087	1.062	1.037
Na_2	1.106	0.943	0.902	0.881	0.881	0.850	0.735
CO	10.622	10.969	11.518	11.569	11.576	11.609	11.108
LiH	2.975	2.684	2.643	2.622	2.612	2.601	2.415
MAE	1.083	0.545	0.097	0.041	0.026	/	/

lengths, as expected, the converged LDA bond lengths are systematically smaller than the corresponding experimental values, while the converged PBE values show the opposite behavior.

3.2.2. Atomization energies

The atomization energy refers to the energy cost to split a molecule into individual atoms. It is an important property in thermochemistry. The benchmark for the atomization energy are done using the same diatomic molecular set and hierarchal atomic orbitals as used for bond-length tests. The results are presented in Table 3. For open-shell atoms, the spin-polarized, symmetry-broken solution usually has the lowest ground-state energy, and is thus taken here as the reference of calculated atomization energy. As can be seen from Table 3, for all molecules, the atomization energies obtained with the atomic basis sets converge systematically towards the PW limit.

Quantitatively, however, the accuracy of atomization energies obtained with atomic basis sets is not so spectacular as the one of geometrical properties. In particular, the atomization energies from SZ basis are indeed too small; the corresponding MAE is over 1 eV. The MAE is improved by about a factor of 2 when the basis set goes from SZ to DZ, but is still far from satisfactory. A dramatic improvement is achieved at the DZP level where a MAE around 0.1 eV is an acceptable accuracy for most practical purposes. Nevertheless, to reach the "chemical accuracy" (1 kcal/mol $\approx$ 0.043 eV), one has to go further in the hierarchy of atomic basis sets. The "chemical accuracy" is almost reached with the TZDP basis (0.034 eV for LDA and 0.041 eV for PBE) and well reached with QZTP (0.022 eV for LDA and 0.026 eV for PBE). Here, the so-called basis-set error is much smaller than the errors of the energy functionals. For this diatomic molecular test set listed in Table 3, on average PBE overbinds by 0.36 eV and LDA overbinds by 0.75 eV by comparing the converged PW results to the experimental ones.

3.2.3. Vibrational frequency

For a given molecule, the equilibrium bond length and the atomization energy reflect the position and depth of the minimum in its potential energy surface, respectively, and the vibrational frequency probes the curvature of the potential energy surface around the equilibrium geometry. The vibrational frequency can be measured directly by experiment and is a powerful probe of structural and bonding characteristics of a molecule.

In Table 4, we present the calculated vibrational frequencies for the same molecular test set and basis sets used before. Compared to the PW reference results, the MAE is reduced dramatically when the basis set goes from SZ to DZP. Specifically, at the DZ level the MAEs are 65 cm^{-1} for LDA and 47 cm^{-1} for PBE, and these numbers are further reduced to 6 cm^{-1} when the basis set increased from the DZ to DZP. The results indicate the importance of polarization functions in an atomic basis set to accurately describe the curvature of the potential energy surface. Nevertheless, unlike the tests for bond lengths and atomization energies of molecules, increasing the size of basis set does not guarantee a better description of these vibrational frequencies. We see that when CGH basis set goes beyond DZ, it still introduces around 6 cm^{-1} error for the vibrational frequencies of molecules comparing to PW calculation results. We suspect that the remaining (almost a constant) error comes from the finite difference approach used in our vibrational frequency calculations, but this still needs to be checked in future. Overall speaking, this accuracy is already excellent for most practical purposes.

3.2.4. Weak interaction energy

In the previous tests, we have demonstrated the convergence behavior of our basis sets for chemically bonded diatomic molecules. In a sense, the good performance of these atomic basis sets for the tested molecules is not surprising, since the homo-nuclear diatomic molecules are the target systems when generating atomic orbitals. Now we turn to the study of bigger and more weakly bonded molecules – the S22 test set [41]. This test set contains 22 weakly interacting molecular complexes that include hydrogen bonding, dispersion interaction, and mixed bonding types. Since its inception, the S22 test set has been widely

Table 4
Vibrational frequencies (in cm^{-1}) of molecules obtained with various sets of atomic orbitals, in comparison with PW and experimental results (EXP). Results from both LDA and PBE are shown. The MAEs are calculated based on the results from atomic basis set and PW basis set.

Molecules	SZ	DZ	DZP	TZDP	QZTP	PW	EXP
LDA							
N_2	1857	2261	2378	2394	2391	2370	2359
O_2	1246	1329	1558	1581	1582	1567	1580
S_2	517	675	717	719	719	721	726
F_2	813	885	920	915	917	924	917
Cl_2	498	524	561	560	562	567	560
$B2_2$	471	382	341	341	339	332	325
I_2	345	234	199	199	201	206	215
Li_2	306	331	342	340	340	339	351
Na_2	129	141	151	148	150	147	159
CO	1631	1998	2130	2130	2130	2130	2170
LiH	1107	1286	1327	1330	1334	1341	1406
MAE	207	69	6	8	7	/	/
PBE							
N_2	1938	2397	2374	2378	2380	2365	2359
O_2	1297	1414	1567	1567	1566	1572	1580
S_2	546	684	721	718	716	723	726
F_2	758	872	914	917	918	920	917
Cl_2	427	517	562	566	564	563	560
$B2_2$	459	374	339	340	333	329	325
I_2	318	249	224	224	222	219	215
Li_2	313	335	345	345	344	342	351
Na_2	132	145	151	151	150	149	159
CO	1728	2075	2147	2149	2147	2144	2170
LiH	1104	1296	1332	1339	1341	1348	1406
MAE	192	48	6	6	5	/	/

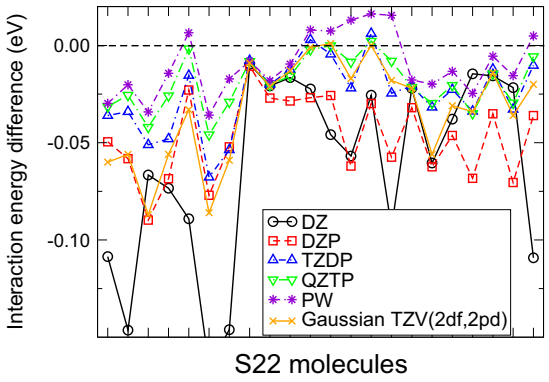

Fig. 3. PBE-D2 interaction energies of the S22 molecules obtained with increasing LCAO basis sets, with reference to the CCSD(T) results (the zero dash line). The results from PW basis set and Gaussian TZV(2df,2pd) (Ref. [47]) basis set are shown for comparison. Lines are used to guide the eye.

Table 5
Lattice constants (in Å) of 20 solids obtained from various LCAO basis sets, compared to the PW and experimental (EXP) results. Experimental data (corrected for zero-point anharmonic effects) are taken from Refs. [51,52].

Solid	SZ	DZ	DZP	TZ(DP)	QZ(TP)	PW	EXP
GaAs	5.63	5.59	5.57	5.55	5.55	5.54	5.64
GaP	5.43	5.40	5.35	5.33	5.34	5.34	5.44
GaN	4.30	4.35	4.40	4.41	4.41	4.41	4.52
InAs	6.01	5.97	5.97	5.96	5.96	5.96	6.05
InP	5.84	5.81	5.79	5.78	5.78	5.78	5.86
InSb	6.46	6.40	6.39	6.39	6.39	6.38	6.47
AlAs	5.76	5.70	5.62	5.61	5.61	5.60	5.65
AlP	5.55	5.51	5.42	5.41	5.41	5.40	5.45
AlN	4.39	4.33	4.29	4.27	4.27	4.27	4.37
C	3.63	3.55	3.51	3.50	3.50	3.50	3.55
Si	5.59	5.53	5.41	5.40	5.40	5.40	5.42
Ge	5.73	5.69	5.64	5.61	5.61	5.61	5.64
LiF	4.15	3.94	3.90	3.88	3.88	3.88	3.97
NaCl	5.62	5.54	5.51	5.50	5.50	5.50	5.57
MgO	3.96	4.02	4.06	4.07	4.07	4.07	4.19
Na (bcc)	3.51	3.94	4.05	4.06	4.06	4.08	4.21
Al (fcc)	3.71	3.81	3.87	3.90	3.91	3.93	4.02
Cu (fcc)	3.26	3.51	/	3.52	3.53	3.53	3.60
Fe (bcc)	2.45	2.58	/	2.72	2.72	2.73	2.86
Ti (hcp)	2.61	2.78	/	2.80	2.80	2.81	2.96
MAE	0.16	0.07	0.02	0.01	0.01	/	/

used to benchmark computational methods that deal with van der Waals (vdW) interactions.

Each member in the S22 test set is a molecular dimer that contains two monomers interacting with each other. The interaction energy is defined as the difference between the total energy of the dimer and the sum of the total energies of the two individual monomers in their fully relaxed geometries. In this work, the interaction energies of the S22 molecules are calculated using the DFT-D2 method of Grimme [47], specifically PBE-D2, as recently implemented in ABACUS.

The calculations for S22 molecules are still done with the supercell approach with cubic boxes that are sufficiently large (up to 50 Bohr side length) to avoid artificial interactions between the molecule and it the periodic images. Fig. 3 presents the interaction energy differences of the S22 molecules calculated from two methods. The first is PBE-D2 with various atomic basis sets and PW basis set, while the second is the coupled-cluster theory with singles, doubles, and perturbative triples [CCSD(T)] [48] in the complete basis set limit. The results of Grimme as reported in Ref. [49], obtained using the Gaussian TZV(2df,2pd) basis set [50], are also plotted in Fig. 3 for comparison. The CCSD(T) reference is indicated in Fig. 3 by the dash line at energy zero. It can be seen that by increasing the number of atomic orbitals, the results from atomic orbitals systematically approach the PW results, and on average get closer to the CCSD(T) references. This trend again validates the transferability of our atomic basis set. The quality of the Gaussian TZV(2df,2pd) is somewhere between the qualities of DZP and TZDP basis sets. Regarding the performance of the PBE-D2 method itself, it can be concluded that the ABACUS package with atomic basis set is very suitable for describing vdW forces.

3.3. Solids

In Section 3.2, we have validated the accuracy of ABACUS with its associated atomic basis sets for molecular properties. Here we turn to the test of crystalline solids. This is a crucial check for the transferability of the atomic basis sets, because they are generated from diatomic systems and are now used to test solid systems. In analogy to the bond lengths, atomization energies, and vibrational frequencies for molecules, here we benchmark the lattice constants, cohesive energies, and bulk moduli for solids.

Twenty crystalline solids are chosen as a test set that covers group III–V and group IV semiconductors, alkaline and alkaline-earth metals, alkaline chloride, as well as transition metals. The lattice constants and bulk moduli of group III–IV and group IV semiconductors obtained using ABACUS have already been reported in Ref. [9]. They are included here for completeness. Since here we are mainly interested in the convergence behavior of the LCAO basis sets instead of the performance of the exchange–correlation functionals, in this test only the LDA is used for simplicity, except for Fe we choose PBE which yields the correct body-centered-cubic (bcc) ground-state crystal structure. For transition metal elements, TZ ($3s3p3d$) and QZ ($4s4p4d$) basis sets are used because adding the polarization functions (f orbitals) does not make a noticeable difference. Note that these TZ/QZ basis sets are grouped together with other TZDP/QZTP basis sets for the statistical error analysis of energy differences in Tables 5–7. Similar to the molecular test case, PW basis results are also reported in these tables as references using the same energy cutoffs and pseudopotentials as in LCAO calculation. The MAEs are obtained between the results from atomic basis sets and the PW basis set. Both simulations were carried by ABACUS.

Monkhorst–Pack (MP) **k**-point meshes are used for the BZ sampling. Specifically, a $4 \times 4 \times 4$ **k**-point mesh is used for semiconductors range from GaAs to Ge. A $6 \times 6 \times 6$ **k**-point mesh is used for LiH, NaCl, and MgO. A denser $10 \times 10 \times 10$ **k**-point mesh is used for metals include bcc Na, face-centered-cubic (fcc) Al, fcc Cu, and bcc Fe. Finally, a $10 \times 10 \times 7$ **k**-point mesh is used for hexagonal-close-packed (hcp) Ti. For transition metals, the semi-core electrons are treated as valence electrons for Ti, but not for Fe and Cu. For the geometry optimization of Ti hcp structure, the optimal c/a ratio is 1.590 by determining the minimum of a two dimensional (a, c) energy landscape, with a and c being the lengths of the lattice vectors in the hcp structure.

3.3.1. Lattice constants

Table 5 shows the lattice constants of tested crystalline solids obtained with our hierarchical LCAO basis sets, in comparison with the PW results, as well as experimental data as collected in Refs. [51,52]. As illustrated in Table 5, the calculated lattice constants of solids converge systematically with respect to the LCAO basis set size. For the tested solids, an MAE of 0.02 Å can be achieved with the DZP basis set, while an MAE of 0.01 Å can be reached at the level of TZ(DP) basis set. This accuracy is comparable to that achieved for bond lengths of molecules, and confirms that the structural properties are well described with the LCAO basis sets.

Table 6
Cohesive energies (in eV/atom) of 20 solids at their equilibrium lattice constants obtained from various LCAO basis sets, compared to the PW and experimental (EXP) results. The experimental data are taken from Ref. [53], corrected for the zero-temperature vibration effect as done in Ref. [51].

Solid	SZ	DZ	DZP	TZ(DP)	QZ(TP)	PW	EXP
GaAs	3.14	3.73	3.99	4.01	4.01	4.01	3.34
GaP	3.42	4.01	4.16	4.18	4.18	4.18	3.61
GaN	4.33	5.03	5.25	5.27	5.28	5.28	4.55
InAs	2.72	3.47	3.78	3.82	3.83	3.84	3.08
InP	3.15	3.95	4.17	4.21	4.21	4.22	3.47
InSb	2.47	3.20	3.48	3.53	3.55	3.55	2.81
AlAs	3.69	4.18	4.34	4.57	4.37	4.37	3.82
AlP	4.08	4.57	4.75	4.77	4.77	4.77	4.32
AlN	5.34	6.29	6.46	6.48	6.49	6.49	5.85
C	8.06	8.53	8.72	8.74	8.75	8.75	7.55
Si	4.08	4.76	5.20	5.22	5.24	5.25	4.68
Ge	3.75	4.24	4.55	4.58	4.59	4.60	3.92
LiF	4.17	4.62	4.88	4.90	4.90	4.90	4.46
NaCl	2.49	3.20	3.51	3.52	3.52	3.56	3.34
MgO	4.63	5.46	5.72	5.74	5.74	5.77	5.20
Na(bcc)	0.98	1.10	1.25	1.27	1.27	1.27	1.12
Al(fcc)	3.18	3.79	3.95	3.96	3.96	3.97	3.43
Cu(fcc)	3.65	4.17	/	4.46	4.48	4.50	3.52
Fe(bcc)	5.54	5.18	/	5.10	5.08	5.08	4.30
Ti(hcp)	4.82	5.24	/	5.33	5.35	5.36	4.88
MAE	0.85	0.26	0.04	0.01	0.01	/	/

Table 7
Bulk Moduli (in GPa) of 20 solids at their equilibrium lattice constants obtained from various LCAO basis sets, compared to the PW and experimental (EXP) results. The experimental data are taken from Ref. [51] except for Fe and Ti (Ref. [54]).

Solid	SZ	DZ	DZP	TZ(DP)	QZ(TP)	PW	EXP
GaAs	66.5	68.3	75.1	76.8	76.8	77.2	76
GaP	80.7	82.3	89.8	94.1	93.7	92.4	89
GaN	187.5	203.8	209.6	207.3	207.9	208.2	210
InAs	59.5	65.8	67.2	67.3	67.2	67.9	60
InP	74.3	75.8	77.2	79.5	80.3	81.4	71
InSb	45.0	48.6	49.9	49.9	50.2	51.4	47
AlAs	62.9	71.4	74.2	74.6	74.6	75.3	77
AlP	70.1	78.5	86.2	87.4	87.7	88.3	86
AlN	192.9	202.7	205.3	208.4	207.8	207.2	202
C	428.7	442.8	459.3	459.4	458.5	458.2	443
Si	72.3	78.2	93.9	93.9	93.5	93.3	99
Ge	53.4	67.3	71.1	72.0	72.8	73.5	76
LiF	44.1	58.5	60.2	61.1	61.3	62.6	70
NaCl	14.7	22.1	29.4	29.6	29.8	30.1	27
MgO	128.6	165.4	167.7	171.9	171.3	170.2	165
Na(bcc)	5.9	6.8	7.0	7.0	7.0	7.1	8
Al(fcc)	70.2	74.9	75.8	76.0	76.0	76.2	79
Cu(fcc)	120.8	147.3	/	149.4	150.2	150.6	142
Fe(bcc)	96.8	160.4	/	161.1	161.8	165.0	170
Ti(hcp)	52.8	113.3	/	122.4	122.9	124.5	110
MAE	21.2	5.8	2.1	1.2	0.8	/	/

In addition, it can be seen that the convergence behavior of the basis sets for simple and transition metal elements are very similar to that for group III–V and group IV elements.

3.3.2. Cohesive energies

The cohesive energies of the tested solids at their equilibrium lattice constants are presented in Table 6. Again, the general trend that the LCAO results systematically approach the PW limit can be observed. It is also interesting to point out that the LCAO basis sets show even better convergence behavior for cohesive energies of solids than atomization energies of molecules. For example, at the DZP level, the MAE is only 0.04 eV for the cohesive energies of solids, compared to 0.09 eV for the atomization energies of molecules. The same behavior holds for higher levels of basis sets such as TZDP and QZTP, where the MAEs of 0.01 eV for solids are also twice smaller than those of molecules.

3.3.3. Bulk moduli

The bulk modulus is another key property of solids, reflecting the variation of the ground-state energy with respect to the unit cell volume around the equilibrium state. In Table 7, the bulk moduli of the tested solid are presented. Compared to the PW results, the SZ basis set yields a large MAE of 21.2 GPa. However, this is quickly reduced to 5.8 GPa at DZ level and 2.1 GPa at DZP levels, this accuracy is sufficiently accurate for most purposes. For basis sets larger than the DZP basis set, the MAEs are further reduced to around 1.0 GPa, which are highly accurate. This convergence behavior of the LCAO basis sets is similar to what was observed for the calculated vibrational frequencies for tested molecules in Section 3.2. In addition, similar to the cases of testing lattice constants and cohesive energies, the quality of the basis sets is equally good for transition metal elements as for main-group elements.

3.4. Si(100) surface reconstruction

In the previous tests for molecules and solids, we have established the reliability of the ABACUS package and the accuracy of its associated LCAO basis sets. Here we test a more "challenging" problem – the reconstruction of the Si(100) surface. This surface is technologically important for fabricating silicon-based devices and has been intensively studied both theoretically and experimentally. Different reconstruction models for the Si(100) surface have been proposed in the past [55–58], and the energy hierarchy among these different reconstructions have been examined by both DFT (LDA) calculations [59] and by quantum Monte Carlo [60] calculations. The small magnitude of energy differences between these reconstructions offers an excellent testing ground for ABACUS with the LCAO basis sets.

Three reconstructions of the Si(100) surface are considered in the work, namely the $p(2 \times 1)$ symmetric [denoted as $p(2 \times 1)$s below], $p(2 \times 1)$ asymmetric [$p(2 \times 1)$a], and $p(2 \times 2)$ reconstructions, as shown in Fig. 4(a–c). It is well known that the Si atoms on the surface layer form dimers to lower the energy of the system by removing one of the two dangling bonds [61]. In the $p(2 \times 1)$s reconstruction structure, the two atoms on the top layer come closer symmetrically, with bond length between them becomes slightly shorter than the nearest neighbor distance in the Si bulk. In the $p(2 \times 1)$a case, the dimers buckle out of the Si(100) surface. Finally, in the $p(2 \times 2)$ case, the buckled dimers change their orientations alternatively (see Fig. 4(c)). Note that another $c(2 \times 4)$ reconstruction exists where the adjacent buckled dimer rows

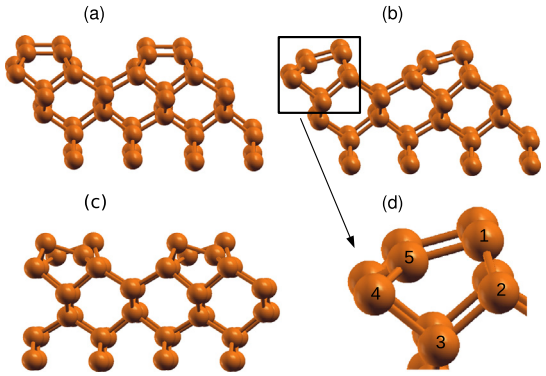

Fig. 4. Side view of three reconstruction structures for the Si(100) surface: (a) $p(2 \times 1)$s; (b) $p(2 \times 1)$a; (c) $p(2 \times 2)$; and (d) zoom-in of the top three layers of the $p(2 \times 1)$a reconstruction structure.

orientate oppositely. However, the energy lowering of this reconstruction is almost identical to that of p(2 × 2) when using DFT with LDA [59], thus this fourth reconstruction structure is not considered in this work.

Next we describe the computational setup of our simulations. ABACUS is used with both LCAO DZP basis set and PW basis set. Also, the Quantum ESPRESSO (QE) package [12] is used, which serves as an independent check for the ABACUS package. The same pseudopotential for Si is used for all three simulations. We model the Si(100) surface by using a repeated slab which contains 12 atomic layers, because the structural distortion below the surface layer extends 4–5 layers into the bulk as noticed before [62]. The central two layers are fixed during the structural relaxation, and only atoms in the outermost five layers on each side are allowed to relax. The conjugate gradient algorithm is used for structural relaxation with a force threshold of 0.01 eV/Å. The slabs are separated by a vacuum of 30 Å thick to avoid artificial interactions between neighboring slabs. When computing the energy differences of the p(2 × 1)s and p(2 × 1)a reconstructions with respect to the ideal surface, the (2×1) unit cell in the *x*–*y* plane is used, while in the case of the p(2 × 2) reconstruction, the (2×2) unit cell is used for both relaxed and ideal surfaces. In all calculations, a (6 × 6 × 1) **k**-point mesh is used.

Table 8 reports the energy lowings of the p(2 × 1)s, p(2 × 1)a, and p(2 × 2) reconstructions with respect to the ideal Si(100) surface. For the ideal Si(100) surface, we fix the surface structure using the bond lengths in Si bulk. Table 8 shows an excellent agreement between the ABACUS/PW results and the QE results. First, from QE calculations, the successive energy decreases of the three relaxation steps, *i.e.,* from the ideal surface to the p(2 × 1)s, p(2 × 1) a, and p(2 × 2) reconstructed surfaces, are 1.504 eV, 0.086 eV, and 0.063 eV per Si dimer, respectively. These numbers can be compared to the 1.80 eV, 0.12 eV, and 0.05 eV ones as reported in Ref. [59]. The differences between results from QE and Ref. [59] are presumably due to the usage of different pseudopotentials, energy cutoff and BZ **k**-point sampling. However, both methods lead to the same energy orderings of the three reconstructions with respect to the ideal Si(100) surface. Also it is assuring that ABACUS with the PW basis set gives almost identical results compared to QE calculations as can be seen in Table 8. Finally, ABACUS with DZP basis set yields 1.481 eV, 0.078 eV, 0.070 eV per Si dimer energy lowerings, which are in excellent agreement with the other two PW results.

Next we examine the relaxed structures obtained by the three methods. We choose the p(2 × 1) reconstruction because its structure distortion is most pronounced among the three. Specifically, we look at the pentagon pattern formed by the atoms from the top three layers of the p(2 × 1) structure, as illustrated in Fig. 4(d). In Table 9, we listed the bond lengths and bond angles (the five edge lengths and angles) of the pentagon as yielded by the three types of calculations. Again, an almost perfect agreement is obtained between the results obtained by the ABACUS/PW calculations and the QE calculation. In this case, the bond lengths from the two methods agree within 0.001 Å, while the bond angles agree within 0.1° (Deg). The results from the DZP basis set are also in excellent agreement with the PW results. The bond lengths from former calculation are slightly longer than the latter ones by 0.003–0.007 Å, and the bond angles differ by 0.4 Deg at most. In conclusion, for all the tested properties of the three reconstructions of Si(100) surface, the ABACUS package with the DZP basis set gives accurate results compared to PW results, demonstrating again the ability of ABACUS to do reliable surface calculations.

Table 8
Energy lowerings per dimer (in eV) of three different reconstructions of the Si(100) surface, with respect to the ideal Si(100) surface.

Surface	ABACUS/DZP	ABACUS/PW	Quantum ESPRESSO
p(2 × 1)s	−1.481	−1.505	−1.504
p(2 × 1)a	−1.559	−1.591	−1.590
p(2 × 2)	−1.629	−1.652	−1.653

Table 9
Bond lengths between the atoms in the top three layers of the p(2 × 1)a reconstruction. a_{ij} is the bond length (in Å) between the *i*-th and *j*-th atoms as shown in Fig. 4(d). θ_i is the bond angle (in Deg.) formed by the two bonds sharing the *i*-th atom.

Parameter	ABACUS/DZP	ABACUS/PW	Quantum ESPRESSO
a_{12}	2.366	2.360	2.360
a_{23}	2.337	2.334	2.335
a_{34}	2.405	2.401	2.401
a_{45}	2.307	2.303	2.302
a_{51}	2.290	2.283	2.283
θ_1	90.13	89.88	89.94
θ_2	104.55	104.24	104.21
θ_3	100.19	99.51	100.49
θ_4	81.34	80.42	80.48
θ_5	121.80	122.15	122.09

3.5. N defect in bulk GaAs

Real materials contain various types of defects, and their presence greatly affects, and often decisively determines the physical properties of materials. In recent years, DFT-based first-principles approaches have emerged as powerful tools for describing and understanding of point defects in solids [63], and is becoming an indispensable complement to experiments that are often difficult and expensive to carry out. Since usually a large supercell is required to model defects in solids, the LCAO technique, which scales favorably with the system size, is a preferable choice for simulating the electronic structures of defects.

As a specific example, we employ the ABACUS package to study the group III–V semiconductor alloy $GaAs_{1-x}N_x$, where *x* is the concentration of the nitrogen impurity. Both GaAs and GaN are technologically important materials in semiconductor industry, hence there has been considerable interest in alloying GaAs and GaN to obtain optoelectronic properties that bridge nitrides and arsenides. The simulations are done again with the supercell approach with successively increasing cell size, containing 16, 32, 64, 128, 256, 512, and finally 1024 atoms. These correspond to approximate *x* values of 0.125, 0.063, 0.031, 0.016, 0.008, 0.004, and 0.002 respectively. Only Γ-point is used in the simulations of supercells with 512 atoms and more. For smaller supercells, finite **k**-point meshes are used. Specifically, they are 1 × 1 × 2, 1 × 2 × 2, 2 × 2 × 2, 2 × 2 × 4, and 2 × 4 × 4 **k**-point meshes for system sizes ranging from 256 atoms to 16 atoms, respectively. The LDA is chosen to be exchange–correlation functional. The internal geometry of each supercell is fully relaxed.

3.5.1. Band gap of $GaAs_{1-x}N_x$

The photoluminescence edge of $GaAs_{1-x}N_x$ for small *x* shows an unexpected redshift, instead of a blueshift [64] as inferred from the linear interpolation between the two endpoints (1.4 eV for GaAs and 3.8 eV for GaN). The narrowing of the alloy band gap $E_g(x)$ from the composition-weighted linear average value $\bar{E}_g(x) = xE_g(0) + (1-x)E_g(1)$ is called the band-gap bowing, which is a general feature of semiconductor alloys and can often be described as $\delta E_g(x) = bx(x-1)$ with *b* being the optical bowing parameter [65]. In $GaAs_{1-x}N_x$, the bowing effect is extremely pronounced with a large *b* coefficient of about 16 eV, in stark contrast with most isovalent semiconductor alloys that have a *b* value of only a fraction of eV. This not only leads to a pronounced

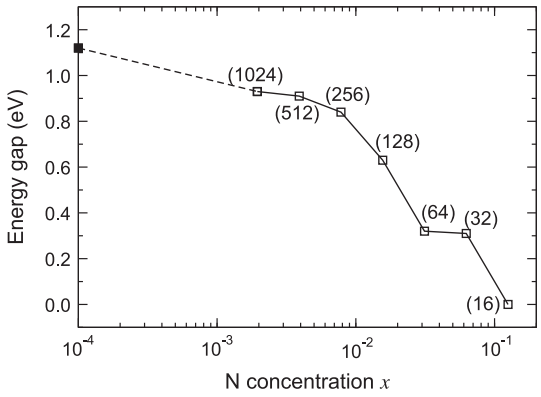

Fig. 5. Calculated band gap of $GaAs_{1-x}N_x$ as a function of the N concentration x. The solid square on the left corresponds to the band gap of GaAs bulk. The number of atoms used in a supercell is labeled for each blank black point. The lines connecting the data points are for guidance.

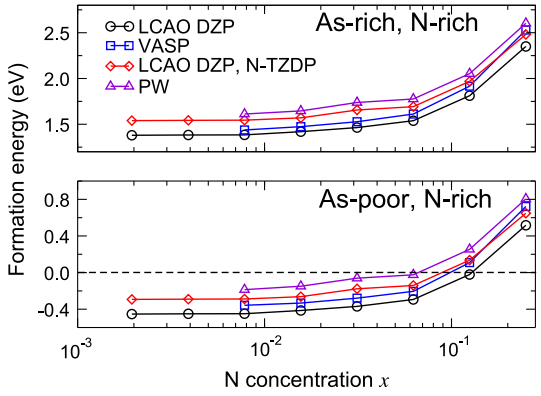

Fig. 6. The N defect formation energy of $GaAs_{1-x}N_x$ as a function of the N concentration x. Two LCAO basis set setups are used in the ABACUS calculations: DZP for all elements (black circles); DZP for Ga and As, and TZDP for N (red diamonds). Results obtained from VASP (blue squares) and ABACUS/PW basis (violet triangles) calculations are shown for comparisons. The energy cutoff is set to 500 eV in VASP calculations. (For interpretation of the references to color in this figure legend, the reader is referred to the web version of this article.)

band-gap narrowing for small x ($x < 0.015$), but also even a closing of the band gap for large x values.

Such a peculiar behavior has been analyzed in details by several theoretical studies [66–69] based on first-principle calculations, and the strong bowing effect has been attributed to the substantial lattice mismatch ($> 20\%$) between GaAs and GaN [66,67] and the formation of spatially separated and sharply localized band-edge states [68]. However, due to the limitation of the computational resources, the previous calculations of $GaAs_{1-x}N_x$ focused only on the alloy regime with $x = 0.25$, 0.50 and 0.75 [66–68], or were based on empirical pseudopotentials [69].

The ABACUS package with LCAO basis sets allows us to reach large systems with x as low as 0.002. The calculated band gaps of $GaAs_{1-x}N_x$ systems are shown in Fig. 5. The blank square points from right to left are the band gaps obtained from supercell calculations using 16, 32, 64, 128, 256, 512, and 1024 atoms, respectively. Note that the $x = 0$ limit represents the calculated band gap of bulk GaAs, which is 1.13 eV from LDA. Although LDA based calculation in general underestimates the band gap of materials, it reproduces very well the experimental finding that the band gap of $GaAs_{1-x}N_x$ gets continuously reduced as x increases. We note that, the geometries of the supercells in this work are chosen in a special way, *i.e.*, by doubling the supercell size successively along the x, y, and z directions. Thus the exact behavior of the plot in Fig. 5 might slightly changes if the shape of the supercells is chosen differently. However, this should not alter the general trend we obtained. We also find that the closing of the band gap happens when x is larger than 0.125.

As a side remark, we noticed that the reported LDA band gaps of bulk GaAs scatter significantly in literatures, ranging from 0.5 to 1.16 eV [70–73]. Our calculated LDA gap is close to the result in Ref. [72], but is noticeably larger than other reported values. A careful analysis reveals that if the semi-core d states of Ga are included as valence electrons in the pseudopotential calculation, the band gap then gets significantly reduced. In addition, the band gap computed at the LDA lattice constant is also appreciably larger than the one computed at the experimental lattice constant (which is larger than the LDA lattice constant), in agreement with the results in Ref. [72]. Since our primary concern here is the capability of ABACUS, and to identify the trend of band gap change of N-doped GaAs, rather than the accurate LDA band gap of bulk GaAs, the cheaper and less accurate Ga norm-conserving pseudopotential was used in our calculation. We however remind the reader that the Ga 3d states should be treated as valence electrons in the pseudopotential calculations if one aims at very accurate LDA band gap of GaAs.

3.5.2. Formation energy of $GaAs_{1-x}N_x$

The next relevant issue is the stability of the $GaAs_{1-x}N_x$ alloy. A key quantity here, for small x, is the formation energy of an N defect, which is defined as

$$E_f = E(Ga_nAs_{n-1}N) - E(Ga_nAs_n) + \mu(As) - \mu(N), \tag{31}$$

where $E(Ga_nAs_n)$ is the energy of a Ga_nAs_n supercell containing n GaAs formula units, $E(Ga_nAs_{n-1}N)$ is the energy of the above supercell but with one As atom replaced by an N impurity atom. $\mu(As)$ and $\mu(N)$ are the chemical potentials for the As atom and the N atom, respectively. The actual value of the atomic chemical potential depends on the chemical conditions in the experiment.

Here we consider two situations: the As-rich & N-rich condition and the As-poor & N-rich condition. In the first one, $\mu(As) = \mu^{rich}(As)$ is chosen to be the energy per atom in the yellow arsenic crystal form. In the second case, $\mu^{poor}(As)$ is given by adding the formation enthalpy of bulk GaAs to $\mu^{rich}(As)$. The formation enthalpy of bulk GaAs bulk is taken here as the atomization energy of GaAs per atom at zero temperature (2.00 eV). Finally, $\mu^{rich}(N)$ is chosen to be one half of the total energy of the N_2 molecule. Obviously, the corresponding N concentration in the supercell $Ga_nAs_{n-1}N$ is given by $x = 1/n$. We would like to point out that, by using Eq. (31), the N impurities are regarded as point defects, and the possible interactions between neighboring N defects are neglected.

In Fig. 6, the formation energy of an N defect is plotted as a function of the N concentration x for both As-rich (upper panel) and As-poor (lower panel) conditions. Calculations are done using the ABACUS package with two sets of LCAO bases: (1) DZP for all elements; (2) DZP for Ga and As, and TZDP for N. The results are compared to those obtained from the ABACUS/PW calculations, and those obtained by the Vienna Ab-initio Simulation Package (VASP) package with projected augmented wave method [74,75]. Fig. 6 shows that under the As-rich condition, the N defect formation energies of $GaAs_{1-x}N_x$ are positive for all N compositions, indicating the very low probability to dope N into GaAs under such condition. However, under the As-poor condition, the formation energies become negative for small N concentrations, which is consistent with the experimental finding that $GaAs_{1-x}N_x$ alloy can only be formed for narrow composition range near the endpoints [64].

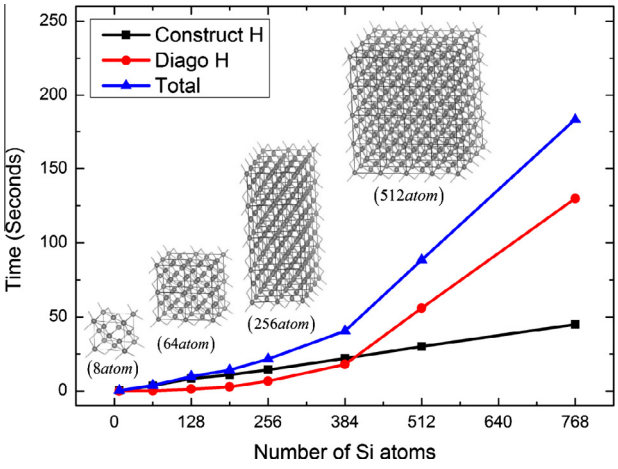

Fig. 7. Scaling behavior of the computational time of one electronic iteration of bulk Si (diamond structure) as a function of the system size. We use eight supercells containing 8, 64, 128, 192, 256, 384, 512, and 768 atoms respectively. For all calculations 8 Intel(R) Xeon(R) CPU cores were used.

The formation energy curves from ABACUS/DZP calculations follow the same trend as the ones from ABACUS/PW calculations for both As-rich and As-poor cases in Fig. 6. However, there are noticeable differences of calculated formation energies between the two methods. Specifically, the formation energies associated with the DZP basis set are underestimated by 0.2–0.3 eV compared to the ones from PW calculations. This is due to the fact that $\mu(N)$ is calculated by half of the N_2 energy (cf. Eq. (31)), and the N_2 total energy calculated with the DZP basis still has an appreciable difference from the PW reference result, as shown in Fig. 2. In fact, by just increasing the N basis set from DZP to TZDP, the corresponding formation energy difference is largely improved to within 0.1 eV compared to PW results for all cases, as shown in Fig. 6. Finally, comparing the ABACUS/PW results and the VASP results reveals that there exists an appreciable difference between the norm-conserving pseudopotential treatment and the projector augmented wave method. Despite these differences, the general trend of the dependence of the formation energy on the N concentration is well reproduced within all calculations.

In conclusion, the study of $GaAs_{1-x}N_x$ alloy illustrates that the ABACUS package with its LCAO basis sets can be used for reliable defect calculations. We would also like to note that, for a thorough and faithful treatment of the phase stability problem of the $GaAs_{1-x}N_x$ alloy, one needs to consider the influence of finite temperatures and include the entropy effect, but this goes beyond the scope of the present work.

3.6. Scaling behavior of the code

An important issue is the computational efficiency of the code. Fig. 7 shows how the computational time of one electronic iteration for bulk Si grows with the supercell size. Calculations were done with 8 CPU cores and the DZP basis set (13 functions for Si) was used. The energy cutoff of the pseudopotential (using LDA) and the cutoff radius of basis functions are listed in Table 1. The data points in Fig. 7 correspond to eight supercells containing 8, 64, 128, 192, 256, 384, 512, and 768 atoms respectively. Only Γ-point was used in the BZ sampling.

For each electronic iteration in the KS-DFT calculation, the computational cost can be splitted into two parts: (1) the construction of the KS Hamiltonian, and (2) the diagonalization of the Hamiltonian matrix. The computational timings for both parts are also given in Fig. 7. For smaller systems (below 200 atoms), the first part dominates while the cost for the second part is significantly smaller than the first. However, the situation changes as the system size keeps increasing: The computational costs of the two parts become comparable at a system size of about 400 atoms, and the diagonalization of the Hamiltonian matrix eventually dominates for even bigger systems. This is because, in our implementations, the cost for the construction of the Hamiltonian matrix scales quasi-linearly with the system size whereas the matrix diagonalization has a canonical scaling of $\mathcal{O}(N^3)$.

Since the rapid increase of the computational cost for systems with more than 400 atoms is due to the matrix diagonalization, we are at the moment working to improve the efficiency of the eigenvalue solver. On one hand, it is possible to interface ABACUS with the ELPA (Eigenvalue SoLvers for Petaflop-Applications) [76] solver, with which we will be able to push the cross point in Fig. 7 to larger systems. On the other hand, the efficiency of PEXSI method in ABACUS has been shown in our previous study [5], we are currently working on integrating the parallel version of PEXSI into ABACUS and a more detailed analysis of the performance of PEXSI within ABACUS will come out in near future. Our near-future goal is to run molecular dynamics simulations for systems with $O(10^3)$ atoms with only modest computer facilities.

4. Summary

To summarize, in this paper we introduce a comprehensive first-principles package, named ABACUS, in which both plane waves and efficient localized atomic orbitals can be used for electronic-structure calculations. In particular, we present the mathematical foundation and numerical techniques behind the atomic-orbital-based implementation within this package. The performance and reliability of the ABACUS package were benchmarked for a variety of systems containing molecules, solids, surfaces and defects. Furthermore, we show that the hierarchial atomic basis sets generated with the CGH scheme allows for a systematic convergence towards the plane-wave accuracy, and the DZP basis set offers an excellent compromise between accuracy and the computational load, and can be used in production calculations for most purposes. The package is currently under active development, with more features and functionalities are being implemented. With all these efforts, we expect the ABACUS package will become a powerful and reliable tool for simulations of large-scale materials.

Acknowledgments

The authors thank Yonghua Zhao and Wei Zhao for the valuable help on the HPSEPS package. LH acknowledges the support from the Chinese National Fundamental Research Program 2011CB921200, the National Natural Science Funds for Distinguished Young Scholars and Chinese National Science Foundation Grant No. 11374275. XR acknowledges the support from Chinese National Science Foundation award number 11374276.

Appendix A

A.1. Two-center integrals

The overlap matrix and the kinetic energy matrix can be efficiently calculated by two-center integral technique [26], which

has been described with full details in Ref. [6]. Here we briefly introduce this algorithm. The overlap matrix is written as

$$S(\mathbf{R}) = \int \phi_\mu^*(\mathbf{r})\phi_\nu(\mathbf{r}-\mathbf{R})d\mathbf{r}, \tag{A.1}$$

which can be further written as [6],

$$S(\mathbf{R}) = \sum_{l=0}^{2l_{max}} \sum_{m=-l}^{l} S_{l_\mu m_\mu, l_\nu m_\nu, lm}(R) G_{l_\mu m_\mu, l_\nu m_\nu, lm} Y_{lm}(\hat{\mathbf{R}}). \tag{A.2}$$

Here $l_\mu(l_\nu)$ and $m_\mu(m_\nu)$ are angular momentum and magnetic quantum numbers for orbital μ (ν). The radial part is

$$S_{l_\mu m_\mu, l_\nu m_\nu, lm}(R) = 4\pi i^{-l} \int_0^\infty j_l(kR) f_\mu(k) f_\nu(k) k^2 dk. \tag{A.3}$$

Here $f_\mu(k)$ and $f_\nu(k)$ are one dimensional Fourier transform of the radial atomic functions introduced in Eq. (15),

$$f_\mu(k) = \sqrt{\frac{2}{\pi}}(-i)^{l_\mu} \int_0^\infty r^2 j_{l_\mu}(kr) f_\mu(r) dr. \tag{A.4}$$

$S_{l_\mu m_\mu, l_\nu m_\nu, lm}(R)$ can be tabulated with dense sampling of distances between ϕ_μ and ϕ_ν. $G_{l_\mu m_\mu, l_\nu m_\nu, lm}$ in Eq. (A.2) is called the Gaunt coefficient,

$$G_{l_\mu m_\mu, l_\nu m_\nu, lm} = \int_0^\pi \sin(\theta) d\theta \int_0^{2\pi} Y_{l_\mu m_\mu}(\theta,\phi) Y_{l_\nu m_\nu}(\theta,\phi) Y_{lm}(\theta,\phi) d\phi, \tag{A.5}$$

which can be calculated and tabulated recursively from the Clebsch–Gordan coefficients [6]. For convenience, the real spherical harmonic functions are actually used in ABACUS. The overlap matrix formed by an atomic orbital $|\phi_\mu\rangle$ and a non-local projector $|\chi_{\alpha lmn}\rangle$ (see Eq. (6)) can be calculated exactly in the same way.

The kinetic energy operator matrix element,

$$T(\mathbf{R}) = \int \phi_\mu^*(\mathbf{r}) \left(-\frac{1}{2}\nabla^2\right) \phi_\nu(\mathbf{r}-\mathbf{R}) d\mathbf{r} \tag{A.6}$$

is slightly different. This term can be calculated in a similar way as $S(\mathbf{R})$ by replacing $S_{l_\mu m_\mu, l_\nu m_\nu, lm}(R)$ with

$$T_{l_\mu m_\mu, l_\nu m_\nu, lm}(R) = 2\pi i^{-l} \int_0^\infty j_l(kR) f_\mu(k) f_\nu(k) k^4 dk. \tag{A.7}$$

Because $S_{l_\mu m_\mu, l_\nu m_\nu, lm}(R)$, $G_{l_\mu m_\mu, l_\nu m_\nu, lm}$ and $T_{l_\mu m_\mu, l_\nu m_\nu, lm}(R)$ are all independent of the coordinates of atoms, they can be tabulated at the beginning of the DFT calculations once for all. For any given distance between two atoms, the corresponding overlap matrix elements and kinetic energy matrix elements can be calculated efficiently by interpolation method.

A.2. Grid-based techniques

The Hamiltonian matrix elements $V_{\mu\nu}^{loc}$ are evaluated on a uniform real space grid, with both atomic orbitals and local potentials presented on each grid point. The local potential is,

$$V^{loc}(\mathbf{r}) = V^L(\mathbf{r}) + V^H(\mathbf{r}) + V^{xc}(\mathbf{r}), \tag{A.8}$$

where $V^L(\mathbf{r}) = \sum_{\mathbf{R}} \sum_{\alpha i} v_\alpha^L(\mathbf{r} - \tau_{\alpha i} - \mathbf{R})$ is the summation of all the local pseudopotentials for i-th atom of element type α. Plane wave basis and Fast Fourier Transform (FFT) techniques are used here to efficiently evaluate $V^L(\mathbf{r})$ and $V^H(\mathbf{r})$ on the grid. Because the local pseudopotential $v_\alpha^L(\mathbf{r})$ has a fairly long tail in real space, it is inefficient to calculate $V^L(\mathbf{r})$ directly on a real space grid. Therefore, $V^L(\mathbf{G})$ is first calculated in reciprocal space as

$$V^L(\mathbf{G}) = \sum_\alpha S_\alpha(\mathbf{G}) v_\alpha^L(\mathbf{G}), \tag{A.9}$$

where $S_\alpha(\mathbf{G}) = \sum_i e^{-i\mathbf{G}\cdot\tau_{\alpha i}}$ is the structure factor. An FFT is carried out to bring $V^L(\mathbf{G})$ back to real space. From our tests, this construction processes of $V^L(\mathbf{r})$ only take a small portion of total computational time, even for systems containing thousands of atoms. This is different from the method used in Ref. [6], where the short-ranged neutral atom potentials are used. Using the same set of plane wave basis, the Hartree potential is also first evaluated in reciprocal space and then be brought back to real space by using an FFT. The full formula of Hartree potential is

$$V^H(\mathbf{r}) = 4\pi \sum_{\mathbf{G}\neq 0} \frac{\rho(\mathbf{G})}{|\mathbf{G}|^2} e^{i\mathbf{G}\cdot\mathbf{r}}. \tag{A.10}$$

A.3. Force calculations

As shown in the main text, the forces evaluated from the basis of atomic orbitals have four contributions,

$$F = F^{FH} + F^{pulay} + F^{ortho} + F^{Ewald}, \tag{A.11}$$

which are the Feynman–Hellmann force, the Pulay force, the force due to nonorthogonality of the atomic orbitals, and the Ewald force due to the Coulomb interactions between the ions. The Ewald force can be calculated analytically using the Ewlad summation techniques [33], and therefore not discussed here. We discuss here the techniques to evaluate the rest three terms as follows.

1. Feynman–Hellmann force,

$$F_{\alpha i}^{FH} = -\sum_{\mathbf{R}} \sum_{\mu\nu} \left\langle \phi_{\mu\mathbf{R}} \left| \frac{\partial H}{\partial \tau_{\alpha i}} \right| \phi_{\nu 0} \right\rangle. \tag{A.12}$$

In Hamiltonian H, only the local and non-local pseudopotentials explicitly depend on the coordinates of ions. Thus we can further break $F_{\alpha i}^{FH}$ into two terms related to pseudopotentials. The first one is related to the local pseudopotential, and can be evaluated in reciprocal space,

$$F_{\alpha i}^{L} = \sum_{\mathbf{G}\neq\mathbf{0}} i\mathbf{G} e^{-i\mathbf{G}\cdot\tau_{\alpha i}} V^L(\mathbf{G}) \rho^*(\mathbf{G}). \tag{A.13}$$

This method has been shown to be accurate and fast [77]. The second term involves the non-local pseudopotential,

$$\begin{aligned} F_{\alpha i}^{NL} &= -\sum_{\mathbf{R}} \sum_{\mu\nu} \left\langle \phi_{\mu\mathbf{R}} \left| \frac{\partial V^{NL}}{\partial \tau_{\alpha i}} \right| \phi_{\nu 0} \right\rangle \\ &= -\sum_{\mathbf{R}} \sum_{\mu\nu} \sum_{lmn} \left(\left\langle \phi_{\mu\mathbf{R}} \left| \frac{d\chi_{\alpha ilmn}}{d\tau_{\alpha i}} \right\rangle \langle \chi_{\alpha ilmn} | \phi_{\nu 0} \right\rangle \right. \\ &\quad \left. + \left\langle \phi_{\mu\mathbf{R}} | \chi_{\alpha ilmn} \right\rangle \left\langle \frac{d\chi_{\alpha ilmn}}{d\tau_{\alpha i}} | \phi_{\nu 0} \right\rangle \right). \end{aligned} \tag{A.14}$$

A non-local pseudopotential projector $\chi_{\alpha ilmn}$ is also a one dimensional numerical orbital like atomic orbital. Therefore, the above equation can be evaluated efficiently using two-center integral technique introduced before.

2. Pulay force.
The existence of Pulay force is due to the fact that the basis set is not complete,

$$F_{\alpha i}^{pulay} = -\sum_{\mathbf{R}} \sum_{\mu\nu} \left(\left\langle \frac{\partial \phi_{\mu\mathbf{R}}}{\partial \tau_{\alpha i}} | H | \phi_{\nu 0} \right\rangle + \left\langle \phi_{\mu\mathbf{R}} | H | \frac{\partial \phi_{\nu 0}}{\partial \tau_{\alpha i}} \right\rangle \right). \tag{A.15}$$

The kinetic energy term and the non-local pseudopotential term in $F_{\alpha i}^{pulay}$ can also be calculated by the two center integral technique, whereas the local potential term is evaluated by the grid integral technique. These steps are similar to the calculations of Hamiltonian matrix, except one needs to substitute ϕ_μ and ϕ_ν

with $\frac{d\phi_\mu}{d\tau_{\alpha i}}$ and $\frac{d\phi_\nu}{d\tau_{\alpha i}}$. To evaluate the derivatives of an atomic orbital with respect to the coordinates of the atoms, one needs to deal with both radial atomic orbital and spherical harmonic function parts. The radial part can be calculated numerically on a one dimensional grid while the second part can be obtained analytically by using the real spherical harmonic functions.

3. The force arises from the fact that atomic orbitals are not orthogonal,

$$F_{\alpha i}^{ortho} = -\sum_{\mathbf{R}}\sum_{\mu\nu} E_{\mu\nu}(\mathbf{R})\frac{\partial S_{\mu\nu}(\mathbf{R})}{\partial \tau_{\alpha i}}, \tag{A.16}$$

where

$$E_{\mu\nu}(\mathbf{R}) = \frac{1}{N_k}\sum_{n\mathbf{k}} f_{n\mathbf{k}}\epsilon_{n\mathbf{k}} c^*_{\mu n,\mathbf{k}} c_{\nu n,\mathbf{k}} e^{-i\mathbf{k}\cdot\mathbf{R}} \tag{A.17}$$

is the element of "energy density matrix" [6]. The derivative of overlap matrix with respect to atomic coordinates is,

$$\frac{\partial S_{\mu\nu}(\mathbf{R})}{\partial \tau_\nu} = -\frac{\partial S_{\mu\nu}(\mathbf{R})}{\partial \tau_\mu} = \frac{dS_{\mu\nu}(\mathbf{R})}{d\mathbf{D}}, \tag{A.18}$$

where τ_μ and τ_ν are the atomic coordinates for orbital μ and ν, and $\mathbf{D} = \mathbf{R} + \tau_\nu - \tau_\mu$, is the distance between two orbitals. The further expansion of this term is

$$\frac{dS_{\mu\nu}(\mathbf{R})}{d\mathbf{D}} = \sum_{lm}\frac{d}{dD}\left[D^{-l}S_{l_\mu m_\mu, l_\nu m_\nu, lm}(D)\right] G_{l_\mu m_\mu, l_\nu m_\nu, lm} Y_{lm}(\widehat{\mathbf{D}}) D^l \widehat{\mathbf{D}} + \sum_{lm} D^{-l} S_{l_\mu m_\mu, l_\nu m_\nu, lm}(D) G_{l_\mu m_\mu, l_\nu m_\nu, lm}\frac{d}{d\mathbf{D}}\left[Y_{lm}(\widehat{\mathbf{D}}) D^l\right]. \tag{A.19}$$

In order to make $Y_{lm}(\widehat{\mathbf{D}})$ analytical at the origin, here it is multiplied by D^l. $\frac{d}{dD}\left(D^{-l}S_{l_\mu m_\mu, l_\nu m_\nu, lm}(D)\right)$ can be calculated numerically using interpolation method while $\frac{d}{d\mathbf{D}}\left[Y_{lm}(\widehat{\mathbf{D}})D^l\right]$ can be calculated analytically by using real spherical harmonic functions.

References

[1] P. Hohenberg, W. Kohn, Phys. Rev. 136 (1964) 864B.
[2] W. Kohn, L.J. Sham, Phys. Rev. 140 (1965) 1133A.
[3] S. Goedecker, Rev. Mod. Phys. 71 (1999) 1085.
[4] L. Lin, J. Lu, R. Car, W. E, Phys. Rev. B 79 (2009) 115133.
[5] M. Chen, G.C. Guo, L. He, J. Phys.: Condens. Matter 25 (2013) 295501.
[6] J.M. Soler, E. Artacho, J.D. Gale, A. Garcia, J. Junquera, P. Ordejon, D.S. Portal, J. Phys.: Condens. Matter 14 (2002) 2745.
[7] T. Ozaki, Phys. Rev. B 67 (2003) 155108.
[8] V. Blum, R. Gehrke, F. Hanke, P. Havu, V. Havu, X. Ren, K. Reuter, M. Scheffler, Comput. Phys. Commun. 06 (2009) 022.
[9] M. Chen, G.C. Guo, L. He, J. Phys.: Condens. Matter 22 (2010) 445501.
[10] M. Chen, G.C. Guo, L. He, J. Phys.: Condens. Matter 23 (2011) 325501.
[11] http://abacus.ustc.edu.cn.
[12] P. Giannozzi, S. Baroni, N. Bonini, M. Calandra, R. Car, C. Cavazzoni, D. Ceresoli, G.L. Chiarotti, M. Cococcioni, I. Dabo, A. Dal Corso, S. de Gironcoli, S. Fabris, G. Fratesi, R. Gebauer, U. Gerstmann, C. Gougoussis, A. Kokalj, M. Lazzeri, L. Martin-Samos, N. Marzari, F. Mauri, R. Mazzarello, S. Paolini, A. Pasquarello, L. Paulatto, C. Sbraccia, S. Scandolo, G. Sclauzero, A.P. Seitsonen, A. Smogunov, P. Umari, R.M. Wentzcovitch, J. Phys.: Condens. Matter 21 (39) (2009) 395502. 19pp. <http://www.quantum-espresso.org>.
[13] http://opium.sourceforge.net.
[14] S. Grimme, J. Comput. Chem. 27 (2006) 1787.
[15] D.R. Hamann, M. Schluter, C. Chiang, Phys. Rev. Lett. 43 (1979) 1494.
[16] L. Kleinman, D.M. Bylander, Phys. Rev. Lett. 48 (1982) 1425.
[17] Delley, J. Chem. Phys. 92 (1990) 508.
[18] S.D. Kenny, A.P. Horsfield, Phys. Rev. B 62 (2000) 4899.
[19] J. Junquera, O. Paz, D. Sanchez-Portral, E. Artacho, Phys. Rev. B 64 (2001) 235111.
[20] E. Anglada, J.M. Soler, J. Junquera, E. Artacho, Phys. Rev. B 66 (2002) 205101.
[21] P.D. Haynes, M.C. Payne, Comput. Phys. Commun. 102 (1997) 17.
[22] C.K. Gan, P.D. Haynes, M.C. Payne, Phys. Rev. B 63 (2000) 205109.
[23] D.S. Portal, E. Artacho, J.M. Soler, Solid State Commun. 95 (1995) 685.
[24] D.S. Portal, E. Artacho, J.M. Soler, J. Phys.: Condens. Matter 8 (1996) 3859.
[25] V. Blum, R. Gehrke, F. Hanke, P. Havu, V. Havu, X. Ren, K. Reuter, M. Scheffler, Comput. Phys. Commun. 180 (2009) 2175.
[26] D.J.N.O.F. Sankey, Phys. Rev. B 40 (1989) 3979.
[27] http://www.sccas.cas.cn/yhfw/rjzy/zmll.
[28] L. Lin, J. Lu, R. Car, W. E, Commun. Math. Sci. 7 (2009) 755.
[29] L. Lin, J. Lu, L. Ying, W. E, C Chin. Ann. Math. 30B (2009) 729.
[30] L. Lin, M. Chen, C. Yang, L. He, J. Phys.: Condens. Matter 25 (2013) 295501.
[31] L. Lin, A. Garcia, G. Huhs, C. Yang, J. Phys.: Condens. Matter 26 (2013) 305503.
[32] J. Harris, Phys. Rev. B 31 (1985) 1770.
[33] P.P. Ewald, Ann. Phys. 64 (1921) 253.
[34] Pulay, Mol. Phys. 17 (1969) 197.
[35] R.P. Feynman, Phys. Rev. 56 (1939) 340.
[36] A.J.T. Salomon, R. Billeter, W. Thiel, Phys. Chem. Chem. Phys. 2 (2000) 2177–2186.
[37] W.W. Hager, H. Zhang, Pacific J. Optim. 2 (2006) 35.
[38] E. Anglada, J.M. Soler, Phys. Rev. B 73 (2006) 115122.
[39] T.L. Beck, Rev. Mod. Phys. 72 (2000) 1041.
[40] J.M. Soler, E. Artacho, J.D. Gale, A. García, J. Junquera, P. Ordejón, D. Sánchez-Portal, J. Phys.: Condens. Matter 14 (2002) 2745.
[41] P. Jurečka, J. Šponer, J. Černý, P. Hobza, Phys. Chem. Chem. Phys. 8 (2006) 1985.
[42] K.P. Huber, G. Herzberg, Molecular Spectra and Molecular Structure, Van Nostrand Reinhold, New York, 1979.
[43] http://cccbdb.nist.gov/.
[44] J. Perdew, A. Zunger, Phys. Rev. B 23 (1981) 5048.
[45] J.P. Perdew, K. Burke, M. Ernzerhof, Phys. Rev. Lett. 77 (1996) 3865.
[46] T. Ozaki, H. Kino, Phys. Rev. B 04 (2004) 69.
[47] S. Grimme, J. Chem. Phys. 124 (2006) 034108.
[48] T. Takatani, E.G. Hohenstein, M. Malagoli, M.S. Marshall, C.D. Sherrill, J. Chem. Phys. 132 (2010) 144104.
[49] S. Grimme, Phys. Chem. Chem. Phys. 8 (2006) 5287.
[50] A. Schäfer, C. Huber, R. Ahlrichs, J. Chem. Phys. 100 (1994) 5829.
[51] J. Harl, L. Schimka, G. Kresse, Phys. Rev. B 81 (2010) 115126.
[52] L. Schimka, R. Gaudoin, J.K.M. Marsman, G. Kresse, Phys. Rev. B 87 (2013) 214102.
[53] M.W. Chase Jr. (Ed.), NIST-JANAF Thermochemical Tables, AIP, New York, 1998.
[54] W.M. Haynes (Ed.), CRC Handbook and Chemistry and Physics, 95th ed., 1994–1995.
[55] J.D. Levine, Surf. Sci. 34 (1973) 90.
[56] J.A. Appelbaum, G.A. Baraff, D.R. Hamann, Phys. Rev. B 15 (1977) 2408.
[57] D.J. Chadi, Phys. Rev. Lett. 43 (1979) 43.
[58] K. Inoue, Y. Morikawa, K. Terakura, M. Nakayama, Phys. Rev. B 49 (1994) 14774.
[59] A. Ramstad, G. Brocks, P.J. Kelly, Phys. Rev. B 51 (1995) 14505.
[60] S.B. Healy, C. Filippi, P. Kratzer, M. Scheffler, Phys. Rev. Lett. 87 (2001) 016105.
[61] R. Schlier, H. Farnsworth, J. Chem. Phys. 30 (1959) 917.
[62] J.A. Appelbaum, D.R. Hamann, Surf. Sci. 74 (1978) 21.
[63] C. Freysoldt, B. Grabowski, T. Hickel, J. Neugebauer, G. Kresse, A. Janotti, C.G. Van de Walle, Rev. Mod. Phys. 86 (2014) 253.
[64] M. Weyers, M. Sato, H. Ando, Jpn. J. Appl. Phys. 31 (1992) L853.
[65] J.E. Bernard, A. Zunger, Phys. Rev. B 36 (1999) 3199.
[66] A. Rubio, M.L. Cohen, Phys. Rev. B 51 (1995) 4343.
[67] J. Neugebauer, C.G. van de Walle, Phys. Rev. B 51 (1995) 10568.
[68] S.-H. Wei, A. Zunger, Phys. Rev. Lett. 76 (1996) 664.
[69] T. Mattila, S.-H. Wei, A. Zunger, Phys. Rev. B 60 (1999) R11245.
[70] R.W. Godby, M. Schlüter, L.J. Sham, Phys. Rev. B 37 (1988) 10159.
[71] F. Gygi, A. Baldereschi, Phys. Rev. Lett. 62 (1989) 2160.
[72] V. Fiorentini, Phys. Rev. B 46 (1992) 2086.
[73] P. Monachesi, A. Marini, G. Onida, M. Palummo, R. Del Sole, Phys. Stat. Sol. (a) 184 (2001) 101.
[74] G. Kresse, J. Furthmüller, Phys. Rev. B 54 (1996) 11169.
[75] G. Kresse, J. Furthmüller, Comput. Mater. Sci. 6 (1996) 15.
[76] A. Marek, V. Blum, R. Johanni, V. Havu, B. Lang, T. Auckenthaler, A. Heinecke, H.-J. Bungartz, H. Lederer, J. Phys.: Condens. Matter 26 (2014) 213201.
[77] N.D.H. Hine, M. Robinson, P.D. Haynes, C.-K. Skylaris, M.C. Payne, A.A. Mostofi, Phys. Rev. B 83 (2011) 195102.